Aus dem Neurowissenschaftlichen Forschungszentrum

der Medizinischen Fakultät Charité – Universitätsmedizin Berlin

DISSERTATION

Role of hilar mossy cells in the CA3-dentate gyrus network

during sharp wave-ripple activity *in vitro*.

zur Erlangung des akademischen Grades

Doctor of Philosophy (PhD)

im Rahmen des

International Graduate Program Medical Neurosciences

vorgelegt der Medizinischen Fakultät

Charité – Universitätsmedizin Berlin

von

Aarti Swaminathan

aus Thanjavur, Indien

Datum der Promotion: 23.06.2019

Contents

1. Abstract

The dentate gyrus (DG) is considered as the hippocampal input gate for the information arriving from the entorhinal cortex. Embedded into the DG network are two excitatory cell types –granule cells (GCs), which receive inputs from the entorhinal cortex, and hilar mossy cells (MCs), which receive input from GCs and feedback projections from CA3 pyramidal cells (PCs). The postsynaptic targets of MC projections are the GCs and hilar interneurons in both ipsilateral and contralateral hemispheres of the brain. The role of MCs during rhythmic population activity, and in particular during sharp-wave/ripple complexes (SWRs), has remained largely unexplored. SWRs are prominent field events in the hippocampus during slow wave sleep and quiet wakefulness, and are involved in memory consolidation and future planning. In this study, we sought to understand whether MCs participate during CA3 SWRs using an *in vitro* model of SWRs. With simultaneous CA3 field potential– and cell-attached recordings from MCs, we observed that a significant fraction of MCs (47%) are recruited into the active neuronal network during SWRs. Moreover, MCs receive pronounced, compound, ripple-associated synaptic input where both excitatory and inhibitory components are phase-coherent with and delayed to the CA3 ripple. Simultaneous patch recordings from CA3 pyramidal neurons and MCs revealed longer excitatory and inhibitory latencies in MCs, supporting a feedback recruitment from CA3. Our data also show that the excitatory to inhibitory charge transfer (E/I) ratio in MCs is higher than in the CA3 PCs, making the MCs more likely to spike during SWRs. Finally, we demonstrate that a significant fraction (66%) of tested GCs receive SWR-associated excitatory inputs that are delayed compared to MCs, indicating an indirect activation of GCs by CA3 PCs via MCs. Together, our data suggest the involvement of mossy cells during SWRs and their importance as a relay for CA3-dentate gyrus networks in this important physiological network state.

.

2. Zusammenfassung

Der Gyrus dentatus (DG) des Hippokampus wird als Eingangsstation für Informationen aus dem entorhinalen Kortex betrachtet. In das DG-Netzwerk sind zwei exzitatorische Zelltypen eingebettet: Körnerzellen, die Signale von dem entorhinalen Kortex empfangen, und Hilus-Mooszellen (MCs), die Signale von Körnerzellen als auch von *feedback*-Projektionen von CA3-Pyramidenzellen (PCs) empfangen. Postsynaptische Ziele von MC-Projektionen umfassen DG Körnerzellen und verschiedene Interneurone in der selben und in der kontralateralen Hemisphäre des Gehirns. Die Rolle von MCs während rhythmischer Populationsaktivität, und insbesondere während Sharp-Wave / Ripple-Komplexen (SWRs), ist bisher weitgehend unerforscht. SWRs sind prominente Ereignisse im Hippocampus während des Tiefschlafs (Slow wave sleep) und des ruhigen Wachzustandes, und sie sind an der Gedächtniskonsolidierung beteiligt. In der vorliegenden Arbeit, untersuchen wir mithilfe eines in-vitro-Modells von SWRs, inwieweit Mooszellen an SWRs in CA3 beteiligt sind. Mit CA3-Feldpotential-Ableitungen und gleichzeitigen ‚cell-attached' Messungen von einzelnen MCs konnten wir beobachten, dass ein wesentlicher Anteil von MCs (47%) während der SWRs in das aktive neuronale Netzwerk rekrutiert werden. Darüber hinaus fanden wir in MCs SWR-assoziierte synaptische Aktivität, bei denen sowohl die exzitatorischen als auch die inhibitorischen Komponenten phasenkohärent und verzögert zur Ripple Oszillation in CA3 auftreten. Simultane *Patch-clamp* Messungen von CA3-Pyramidenzellen und MCs zeigten längere exzitatorische und inhibitorische Latenzzeiten bei MCs, was die Hypothese einer von CA3 ausgehenden *Feedback*-Rekrutierung unterstützt. Unsere Daten zeigen zusätzlich, dass das Verhältnis exzitatorischer zu inhibitorischer Aktivität in MCs höher ist als in CA3-Pyramidenzellen, wodurch die MCs mit höherer Wahrscheinlichkeit während SWRs überschwellig aktiviert werden. Schließlich zeigen wir, dass ein signifikanter Anteil (66%) der getesteten Körnerzellen SWR-assoziierte exzitatorische Signale erhalten, im Vergleich zu MCs zeitlich verzögert, was auf eine indirekte Aktivierung von Körnerzellen durch CA3 PCs über MCs hinweist. Zusammengefasst zeigen unsere Daten die aktive Beteiligung von Mooszellen an SWRs und deuten auf eine funktionelle Bedeutung als Schaltstelle für das CA3- Gyrus dentatus Netzwerk in diesem wichtigen physiologischen Netzwerkzustand hin.

3. Introduction

The hippocampal formation is involved in higher brain functions such as spatial navigation, encoding of episodic memories, consolidation and future planning (Ólafsdóttir et al., 2018). The dentate gyrus (DG), the input region of the hippocampus, acts as a preprocessor receiving information from the entorhinal cortex and providing the major excitatory input to the CA3 region via the mossy fibers of granule cells (GCs) (Cajal, 1911; Henze et al., 2000). Mossy cells (MCs), the major glutamatergic cells located in the hilar region, receive synaptic inputs mainly from the GCs, hilar interneurons, and also excitatory projections from CA3 pyramidal cells (PCs) (Amaral, 1978; Soriano and Frotscher, 1994; Scharfman et al., 1990; Acsády et al., 2000; Scharfman, 1994). These cells have their dendrites confined mostly to the hilar region (Frotscher et al., 1991). However, dendrites of some MCs extend into the molecular layer where they are likely to receive inputs from entorhinal cortex directly (Scharfman, 1991) or indirectly via semilunar granule cells (Williams et al., 2007; Larimer and Strowbridge, 2010). The MC axons project to the local hilar interneurons (Larimer and Strowbridge, 2008) and to the inner molecular layer of the ipsilateral and contralateral DG (Berger et al., 1981, Ribak et al., 1985; Buckmaster et al., 1996; Hsu et al., 2016). These anatomical features place the mossy cells in a strategic location to mediate a distinct excitatory feedback loop in the DG-CA3 network. The important functional role of mossy cells is evident from the significant neuronal loss observed in temporal lobe epilepsy (Margerison J and Corsellis J, 1966; Ratzliff et al., 2002; Scharfman, 2016).
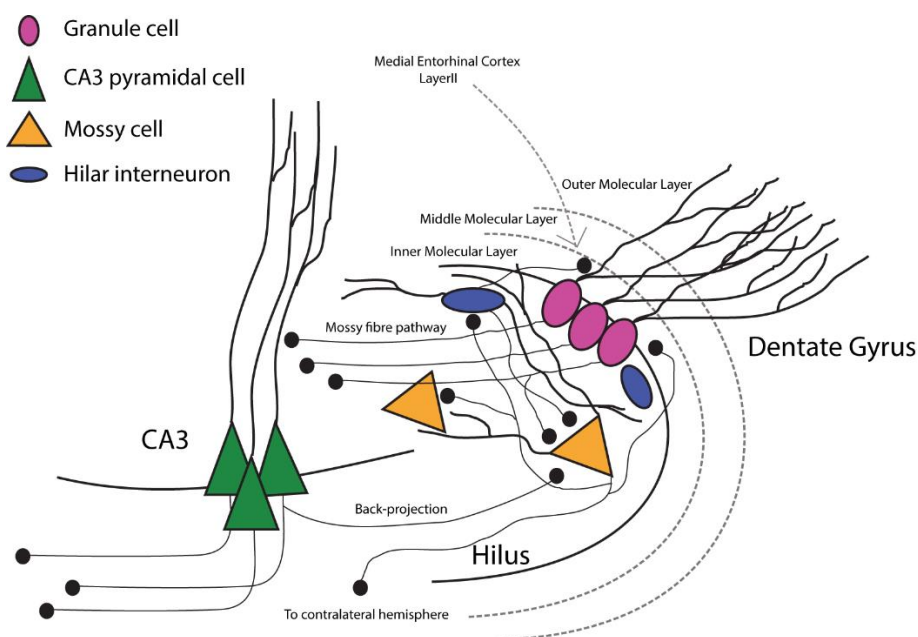
Figure 1: Schematic showing DG-hilar-CA3 network and the anatomical connections between different cell types.

Discrete spatial representations from the entorhinal cortex are thought to be decorrelated by GCs in DG by the process of 'pattern separation', which in turn recruits different CA3 cell assemblies (Leutgeb et al., 2007). The hilus, especially MCs, plays a crucial role in distinguishing closely related patterns as shown by computational models (Myers and Scharfman, 2009; Danielson et al., 2017). Indeed, targeted removal of MCs in mice showed impaired contextual discrimination and increased anxiety-like behaviors (Jinde et al., 2012). During spatial exploration, MCs have been shown to exhibit multiple place fields and undergo remapping of place fields in response to different environments (Senzai and Buzsaki, 2017; Goodsmith et al., 2017; Danielson et al., 2017).

Recent studies have shed more light on the activity of dentate GCs and hilar MCs during different sleep stages in behaving rodents (Neunuebel and Knierim, 2012; Senzai and Buzsaki, 2017; Goodsmith et al., 2017). In particular, MCs have been shown to have higher firing rates during non-rapid eye movement (NREM) states than awake or rapid eye movement (REM) states (Senzai and Buzsaki, 2017; Goodsmith et al., 2017). NREM or slow wave sleep and quiet wakefulness are characterized by transient field events in the CA3 and CA1 regions of the hippocampus termed sharp-waves, which are accompanied by high-frequency (~120-300 Hz) ripple oscillations (Sharp wave ripple complexes [SWRs]) (Buzsáki, 1986; Buzsáki 2015). Neuronal sequences, previously active during behavior, are reactivated during SWRs in the CA1 and CA3 regions (Wilson and McNaughton, 1994; Lee and Wilson 2002). This replay is believed to be the basis for memory consolidation involving information transfer from hippocampus to the neocortex (Girardeau et al., 2009). It remains elusive how the input gate of the hippocampus, the DG and hilus, might mediate entorhinal cortex- hippocampal interactions during NREM sleep. The activity of MCs in the context of different brain rhythms remains to be investigated, with only few studies carried out in anesthetized rats (Soltesz et al., 1993; Henze et al., 2007).

Aims of the project:

During the course of the project, we aimed to understand the involvement of mossy cells during SWRs by studying the firing properties and synaptic inputs in MCs during spontaneous SWRs *in vitro*. To this end, we carried out cell attached/on-cell recordings and whole cell recordings from MCs. In addition, we performed simultaneous whole-cell recordings in CA3 PCs and MCs to determine the timing of synaptic inputs in mossy cells with respect to CA3 PCs. Finally, we recorded from dentate GCs to study the propagation of SWRs into the dentate gyrus possibly via MCs.

4. Materials and Methods

4.1. Slice Preparation

C57BL/6N male mice (3–5 weeks) were decapitated in isoflurane anesthesia in accordance with the institutional guidelines (as approved by the State Office of Health and Social Affairs Berlin LaGeSo (T0100/03), the animal welfare regulations of Charité and the EU Council Directive 2010/63/EU). Brains were transferred to ice-cold sucrose-based ACSF containing (in mM): 87 NaCl, 2.5 KCl, 3 $MgCl_2 \cdot 6H_2O$, 0.5 $CaCl_2$, 10 glucose, 50 sucrose, 1.25 NaH_2PO_4, and 26 $NaHCO_3$ (pH 7.4). Horizontal slices (400 μm) of ventral to mid-hippocampus were cut on a vibratome (VT1200S, Leica) and stored in an interface chamber perfused with ACSF containing (in mM): 119 NaCl, 2.5 KCl, 1.3 $MgCl_2$, 2.5 $CaCl_2$, 10 glucose, 1.25 NaH_2PO_4, and 26 $NaHCO_3$, at pH 7.4; osmolarity of 290 to 310 mOsmol/l. The temperature was kept at 32-34°C, and slices were superfused at a flow rate of ~1 ml/min. ACSF was equilibrated with carbogen (95% O_2, 5% CO_2). Before revordings, slices recovered for at least 1.5 h after the preparation.

4.2. Electrophysiology

Recordings were performed in ACSF at 31-32°C in a submerged-type recording chamber perfused at 5-6 ml/min (Maier et al., 2009). For local field potential (LFP) recordings, glass microelectrodes (tip opening ~5-10 μm; 0.2-0.3 MΩ) were filled with ACSF. Whole-cell recordings were performed with glass electrodes (2-5 MΩ) filled with either of two solutions, containing (in mM): *(i)* 120 K-gluconate, 10 HEPES, 10 KCl, 5 EGTA, 2 $MgSO_4 \cdot 7H_2O$, 3 MgATP, 1 Na_2GTP, 14 phosphocreatine, and 5.4 biocytin (0.2 %); pH adjusted to 7.4 with KOH, or *(ii)* 117.5 gluconic acid, 8 NaCl, 10 TEA, 10 HEPES, 0.2 EGTA, 5 QX-314, 2.5 CsCl, 0.3 Na_2GTP, and 4 MgATP, 5.4 biocytin (0.2%); pH adjusted to 7.4 with CsOH. MC spiking was recorded for at least 10 min either in the cell-attached configuration (voltage clamp, VC, at -60 mV) using solution *(i)* or in on-cell configuration using ACSF-filled patch pipettes. LFPs were amplified 1000× and whole-cell data were amplified 5× for VC and 10× for current-clamp recordings using a Multiclamp 700A or B amplifier (Molecular Devices). Data were low-pass filtered at 4 kHz (Bessel filter) and digitized at 20 kHz with 16-bit resolution using an A/D converter (BNC-2090 board, National Instruments, or Axon Digidata 1550A, Molecular Devices). Data were stored using Igor Pro 6.12 (Wavemetrics) or pClamp (Molecular Devices). Series resistance (R_s) was monitored continuously; recordings were rejected if R_s exceeded 20 MΩ or varied >30%. No R_s compensation was used; no liquid junction potential correction was applied. In on-cell recordings, a candidate MC was chosen, and an ACSF-filled patch pipette placed on its soma. After recording of a sufficient amount of data,

the pipette was removed and the cell re-approached with a new pipette filled with intracellular solution and subsequently recorded in the whole-cell configuration. The depth distribution of the recorded cells from the surface of the slice ranged from 32 to 80 μm.

4.3.   Anatomical identification and immunostainings.

Mossy cells were putatively identified using DIC (differential interference contrast) imaging as multipolar cells with large soma located deep in the hilus and away from CA3c pyramidal layer as described previously (Buckmaster et al., 1993). Cells were routinely filled with 0.2% biocytin and slices were transferred to 4% paraformaldehyde for at least 3 h and maintained at 4° C in 0.1 M phosphate-buffered saline (PBS) with 0.1% sodium-azide. For immunostainings, slices were washed 3 times, 5min each with 0.1 M PBS. The slices were blocked with 5% normal goat serum, followed by overnight incubation with Streptavidin (1:500, Invitrogen) and mouse anti-GAD67 antibody (Ab) (1:500, Millipore) at 4° C. Slices were then washed 3 times 5 min each in 0.1M PBS and incubated in Alexa 488 goat anti-mouse secondary Ab (1:500, Invitrogen), and Alexa 647 goat anti-mouse Ab (1:500, Invitrogen) for 2-4 h at room temperature. After washes in 0.1 M PBS, slices were mounted on slides and embedded in a mounting medium (Mowiol). Z-stack images were taken using a confocal microscope (Leica DMI 6000) with a 20× oil immersion objective and maximum intensity projection images were obtained. Reconstructions were performed using the Simple Neurite Tracer plugin in ImageJ (V 1.51). The identity of the recorded MCs was morphologically confirmed, with many cells having an axon collateral extending towards the s.*oriens* of CA3c as shown previously (Scharfman, 2013; Soltesz 1993). In addition, immunostainings against GAD67 were carried out to exclude hilar interneurons. Neurons labeled positive for GAD67 were excluded from further analysis.

4.4.   Data Analyses

4.4.1 Analyses of intrinsic cellular parameters

Initial resting membrane potential (RMP) was determined in current-clamp immediately after rupturing the cell membrane. *Input resistance* (R_i) was calculated based on -4 mV steps (50 ms duration) in voltage-clamp, repeated 100 times to minimize the influence of spontaneous synaptic inputs. Trace segments of 10 ms duration with minimal standard deviations (SD) for baseline and steady-state were chosen, averaged, and the difference was determined (ΔI). The voltage step size (-4 mV) was then divided by ΔI to calculate the cell's R_i. *Action potential* (AP) parameters were determined from spikes recorded at rheobase. *AP threshold*, V_{thres}: the membrane potential where dV/dt of the rising phase exceeded 20 mV/ms; *peak amplitude* of APs: measured from V_{thres} to the peak; *width* of APs: the difference between the time points where the rise- and the decay phases

intersected 50% of the AP peak amplitude; *after hyperpolarization* amplitude: the voltage difference between V_{thres} and the most negative deflection immediately following the peak of the AP; *sag potential* amplitude: the voltage difference between the minimum voltage in response to the current injection (-120 pA, 1 s) from the RMP and the steady-state response. The intrinsic properties are comparable to those described (Kowalski et al., 2010) and distinct from those of the hilar interneurons (Hosp et al., 2014).

Intrinsic physiological properties of mossy cells	
Resting membrane potential (mV)*	-60.1 ± 1.4
Input resistance (MΩ)	312.8 ± 30.7
Action potential	
Threshold (mV)	-40.0 ± 0.8
Amplitude (mV)	70.5 ± 2.8
Duration at 50% of AP maximum (ms)	0.9 ± 0.03
Afterhyperpolarization amplitude (mV)	6.5 ± 0.8
Sag potential amplitude (mV)	7.0 ± 0.8

*no LJP correction; Values are expressed as mean ± S.E.M.; n = 12 MCs N = 7 mice
95% CIs: RMP: [-63.1 mV -57.1 mV]; Ri: [245.3 MΩ 380.4 MΩ]; AHP: [4.7 mV 8.3 mV]

4.4.2 SWR detection

SWR detection was performed in Matlab (Mathworks) as described previously (Maier et al., 2009). Time windows of 300 ms (55 ms for spike analysis) aligned to the peak of identified SWRs were cut out from LFP- and corresponding intracellular traces and were baseline-corrected by subtracting the respective means. Digital filtering was performed with a 2nd order Butterworth filter at the indicated frequencies.

4.4.3 Analysis of spiking

Spike times were determined using a threshold algorithm (8 times SD of the spike-free baseline). To quantify SWR-related spiking, the number of spikes in n SWR epochs of 55 ms centered on the ripple maxima were determined. This dataset (N_1) was compared with spiking in n periods of trace with identical duration, randomly sampled from the entire spike-train (N_2) (periods with or without SWR epochs; Mann-Whitney U test; α=0.001). As a result, MCs were classified as responding or nonresponding during SWRs. The SWR maximum is the temporal reference in peri-event time histograms (PETHs) (bin width 5 ms; Fig. 2H). The sum of spike counts S per time bin were divided by the sum of SWRs m observed, and the bin width Δt, indicating spike rates ($SR=S/m/\Delta t$, *i.e.* the probability to observe a spike in a single trial for the chosen 5 ms time interval).

4.4.4 Analysis of synaptic inputs

Synaptic inputs were detected by a derivative-peak time method (Fig. 5). SWR-related cEPSCs and inverted cIPSCs were low-pass filtered at 400 Hz and the derivative calculated. Of all derivative minima detected within a 60 ms window centered on the maximum of the ripple, the top 10% slopes (*i.e.*, 10% steepest slopes) were accepted as synaptic inputs. LFP signals were filtered at 127–300 Hz. Envelope and phase of the filtered signals were obtained by applying the Hilbert transform. The phase of excitatory or inhibitory inputs was determined as the respective Hilbert phase of the LFP at the time point of the steepest slopes. For each cell, an average phase vector described by its phase angle and strength was determined; the polar plots represent the resultant phase vectors of all analyzed cells.

Timing of cPSCs in double recordings was analyzed in a window of 15 ms surrounding the SWR maximum. Only significant SWR-related inputs were considered, and their delays at the time points of half-maximum amplitudes determined. *The time-dependent power spectrum* of the signal was computed by Morlet wavelet transform (Torrence and Compo, http://atoc.colorado.edu/research/wavelets/). Data are plotted as log(1+power). Frequency at maximum power is defined as the local maximum in the 127-300 Hz range.

4.4.5 Input- and Amplitude-time-histograms

Input-time histograms : For all cells, the mean histogram over events (bin size = 0.1 ms, 400 bins) was generated and normalized, corresponding to the empirical time-dependent input rate (number of inputs/ms). The resulting histograms were averaged and smoothed with a Gaussian kernel (*black lines,* variance 0.2 ms). *Amplitude-time histograms:* Following the detection of the steepest slopes, the absolute amplitudes within the cPSCs were defined as the maximum values of the raw signal in the interval between the steepest increase (*i.e.*, the peak of the cPSC derivative) and the onset of the next synaptic input (*i.e.*, the following minimum of the cPSC derivative). The data were then binned in 2D histograms (Fig. 5C-D, *bottom*): The *x*-axis is the time difference of the steepest increase and the maximum peak of the LFP ripple signal (bin size 0.4 ms, 100 bins). The *y*-axis is the absolute amplitude (bin size 14 pA, 100 bins). The histogram was smoothed by convolution with a 2D Gaussian kernel (kernel width=1.5 bins; variance: 0.6 ms in *x*-axis and 21 pA in *y*-axis). To average over all cells, a histogram was generated for each cell with the sum over all bins normalized to 1, and then the average of all individual histograms was calculated. For calculation of the temporal evolution of cEPSC-to-cIPSC phase difference, the excitatory and inhibitory traces were averaged and their Hilbert phases subtracted for each slice (Fig. 5E).

6

4.4.6 Synaptic inputs in Granule cells

Synaptic inputs in GCs associated with SWRs are smaller on average than those observed in MCs. To separate spontaneous (not SWR-associated) and SWR-associated synaptic inputs, we used the following unbiased procedure to identify 'significant', *i.e.*, SWR-driven synaptic responses. We considered time periods of 2 s centered on the maximum of the ripple peak (127-300 Hz filtered signal). Following baseline offset correction, the current sweeps were divided into 20 ms bins and the mean values were determined in each of the resulting 100 bins. With these values, a matrix of dimension 100× the number of SWR events in the given recording was created. Using repeated measures one-way ANOVA, all matrix elements were pair-wise compared. If the matrix entries within SWR-related bins were determined larger than those in the surrounding bins (determined with Tukey's *post-hoc* test at a level of $\alpha = 0.05$), the given GC was categorized as significantly modulated by SWR-related activity (Fig. 9A, B).

4.4.7 Synaptic input fidelity.

To quantify whether a given individual SWR event evoked a synaptic response in a cell (MC or GC) or not, we statistically compared the current trace surrounding the SWR peak time (-20 ms to +45 ms) to a concatenated current trace containing data clearly separate from this SWR event (-120 ms to -20 ms, and +45 ms to +120 ms with respect to the SWR peak; 175 ms duration). An unpaired two-sample, one-tailed *t* test, with α set to 0.1 was applied (right- and left tailed testing for cEPSCs and cIPSCs, respectively). If the null hypothesis was rejected at $\alpha = 0.1$, the current sweep was classified as containing a synaptic event caused by the given SWR event or was otherwise categorized uncoupled.

4.4.8 Statistics

Statistical analysis was performed in Matlab (Mathworks) or GraphPad Prism. Data are reported as means ± SEM, or medians. Boxplots display the median and margin of error as the 10th and 90th percentiles. Comparisons were made using the two-tailed unpaired or paired *t*-test, the Mann-Whitney *U*-test, or by ANOVA. The uniformity of phase angles was tested using Rayleigh's test with the CircStat toolbox (Berens, 2009) in Matlab. Fisher's *Z* transform was applied before comparing populations of correlation coefficients (Bortz and Schuster, 2010). Statistical significance is given as exact *P* values with $\alpha \leq 0.05$ regarded as significant, unless stated otherwise.

5. Results

5.1 Activation of mossy cells during CA3 sharp wave-ripples

Mossy cells in the hilus have been recently described to be active during spatial exploration and slow wave sleep (Senzai and Buzsaki, 2017). However, the activity of these cells during hippocampal SWRs has not been elucidated, given the anatomical back projection from the CA3 region to MCs (Scharfman, 1994). We used an acute hippocampal slice model of SWRs to study neuronal network mechanisms underlying MC activity. The identity of the recorded cells was confirmed based on morphological (characteristic thorny excrescences on the proximal dendrites) and electrophysiological features (Fig. 2). To study the spiking of the MCs without affecting the intracellular millieu, we performed simultaneous cell-attached or on-cell recordings from MCs with the local field potential (LFP) in the pyramidal cell layer of area CA3c closer to the hilus (as described by Lorente de Nó, 1934) (Fig. 3A). The MCs showed a wide range of overall firing rates (mean: 0.5±0.1/s; median: 0.2/s, range: 0 to 3.6/s; *n*=38 cells).
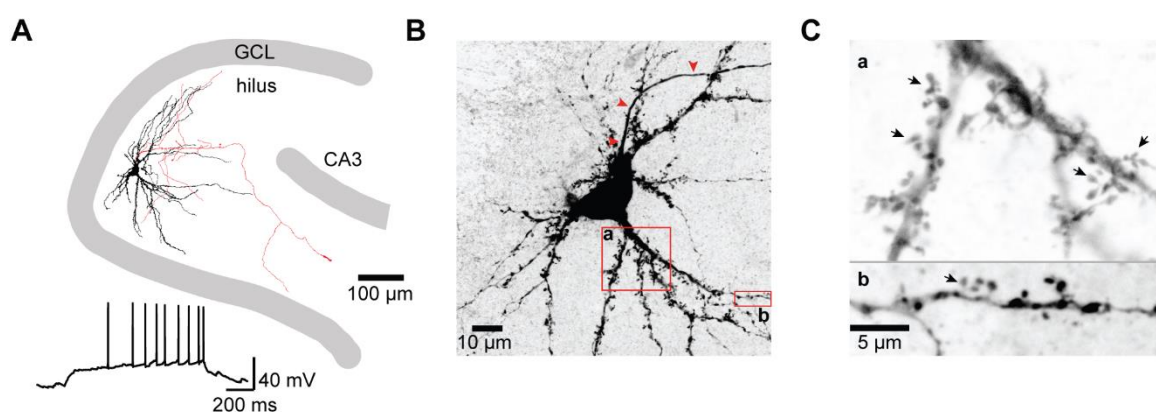

Figure 2: Identification of MCs. A. Reconstruction of a biocytin-filled mossy cell with dendrites in black, and axon in red extending towards stratum oriens. *Below:* Firing pattern during a 40 pA (1 s) current injection. **B.** Maximum projection image of a MC showing complex spines on the proximal dendrites. *Arrowheads* mark the axon. **C.** Magnification of the boxed areas in *B* to visualize spines at higher resolution.

We wondered if the spiking observed in MCs was linked to network activity in the neighbouring CA3 region. Indeed, we observed spikes coinciding with SWRs in a substantial fraction of MCs (47%), suggesting recruitment of these neurons by population activity in the CA3. The coupling of MC spiking during SWRs was statistically evaluated by comparing the spiking during SWRs with spiking during randomly sampled periods using Mann-Whitney *U* test. The spiking in 18 cells (47%) was significantly coupled with SWRs ('responding'), while for the remaining 20 cells (53%), no coupling could be found, or they were mostly silent ('non-responding'; Fig. 3C). In the responding MCs, SWR-linked spiking for individual cells varied between ~5% and 100% (Fig.

3D), independent of the recording depth from the slice surface. The number of spikes per SWR ranged from one to four (mean: 1.4±0.02, Fig. 3E), with some cells showing bursts (Fig. 3B). The spike times in MCs were analyzed with respect to the SWR peak time as a temporal reference across cells. The SWR-locked peri-event time histograms (PETHs) and the averaged PETH after normalization revealed a delayed spiking in MCs (6.4 ms) with respect to the CA3 SWRs (Fig. 3G-H).

We next asked what could account for the differences in responding and non-responding MCs. Therefore, we tested several intrinsic parameters such as resting membrane potential, input resistance, action potential (AP) threshold, AP half duration, after-hyperpolarization amplitude, sag potential amplitude and network parameters such as excitatory, and inhibitory charge transfers, excitatory to inhibitory charge transfer (E/I) ratio. None of these measures was different (see Suppl. Fig. 2 in the paper) with the exception of AP threshold, which was
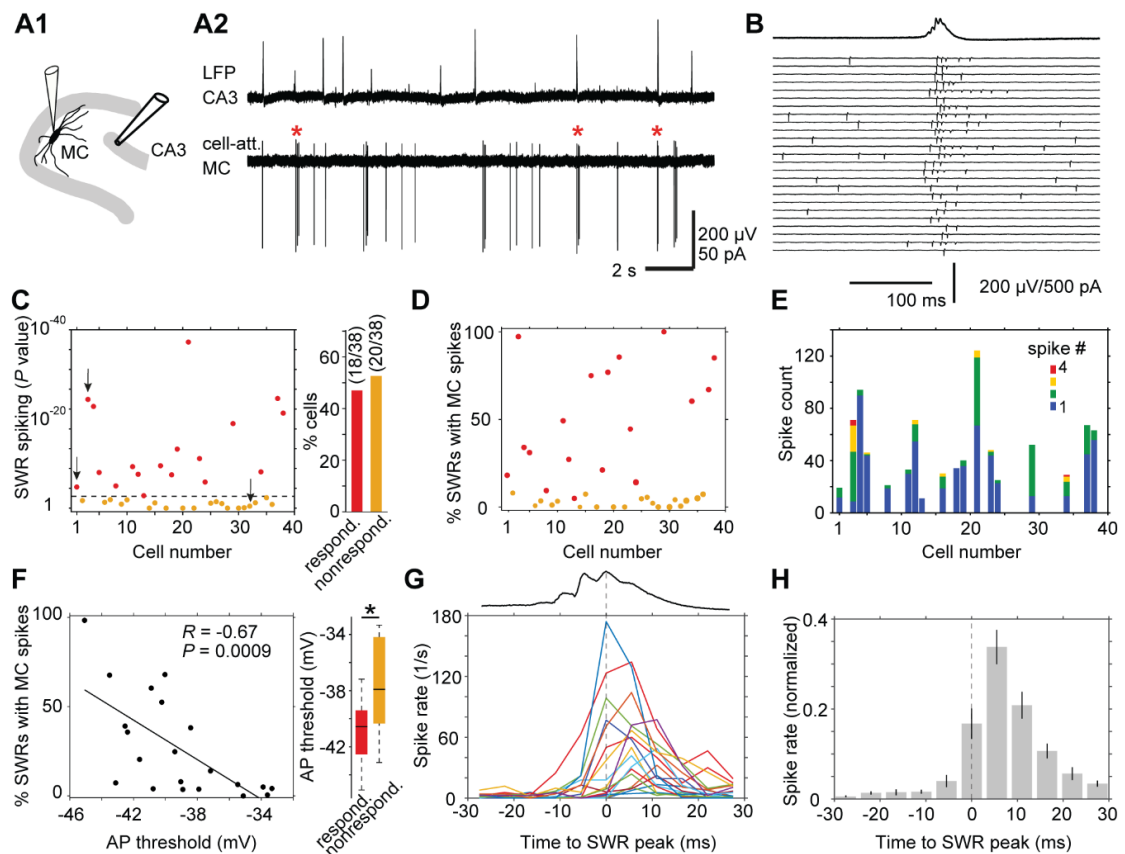

Figure 3: Spiking in MCs during CA3 SWRs. A1. Schematic of parallel LFP- cell attached MC recordings. **A2.** Example showing the CA3 LFP and MC spiking concurrently with SWRs (asterisks). **B.** Discharge patterns of an MC during CA3 SWRs. Successive sweeps (25, 400 ms) centered to the SWR peak (average *top*). **C.** Spiking of MCs within- and outside SWR epochs was compared (Mann-Whitney *U* test). *Left*: display of *P* values (*x*-axis, order of experiments). *Red* and *orange* dots indicate responding and non-responding cells respectively; dotted line: *α*=0.001. *Right:* percentage of responding and non-responding MCs. **D.** Percentage of SWR epochs with MC spiking (*x*-axis

and colour as in *B*). **E.** Distribution of mean spike counts per SWR for responding cells (order as in *B* and *C*). **F.** *Left*, Correlation of MC spiking and AP threshold (*n*=21). *Right:* Comparison of AP threshold in responding and non-responding cells. **G.** PETHs of responding MCs, 5 ms binsize. *Top*: grand average SWR. **H.** Average PETH after normalization (peak at 6.4 ms).

negatively correlated with SWR-related spiking (Fig. 3F). The AP threshold was more negative in responding MCs, implying that these MCs have a higher propensity to spike during SWR- related synaptic inputs (*P*=0.017, two-tailed unpaired *t*-test, Fig. 3F).

5.2 SWR-associated synaptic inputs in mossy cells

Given the SWR-coupled spiking, we were interested to study the underlying synaptic inputs in MCs. Following the cell-attached or on-cell recordings, we recorded compound excitatory and inhibitory postsynaptic currents (cEPSCs at -60 mV, cIPSCs at +6 mV) from the same cells concurrently with CA3 SWRs. MCs received prominent SWR-associated excitatory and inhibitory cPSCs (cEPSCs: mean: 644±70 pA, median: 679 pA; cIPSCs: mean: 509±50 pA, median: 520 pA; *n*=25 cells, Fig. 4A1,B1). Moreover, SWR-related cPSCs in MCs were highly reliable with success rates of 100% and 97% for cEPSCs and cIPSCs. Frequency spectra of cEPSCs and cIPSCs, computed using Morlet wavelet transform, revealed components in the ripple frequency range (cEPSCs *vs* cIPSCs, mean: 144±1 Hz *vs* 144±2 Hz; medians: 143 Hz *vs* 142 Hz; *P*=0.9, Mann-Whitney *U*-test; Fig. 4A2,B2).
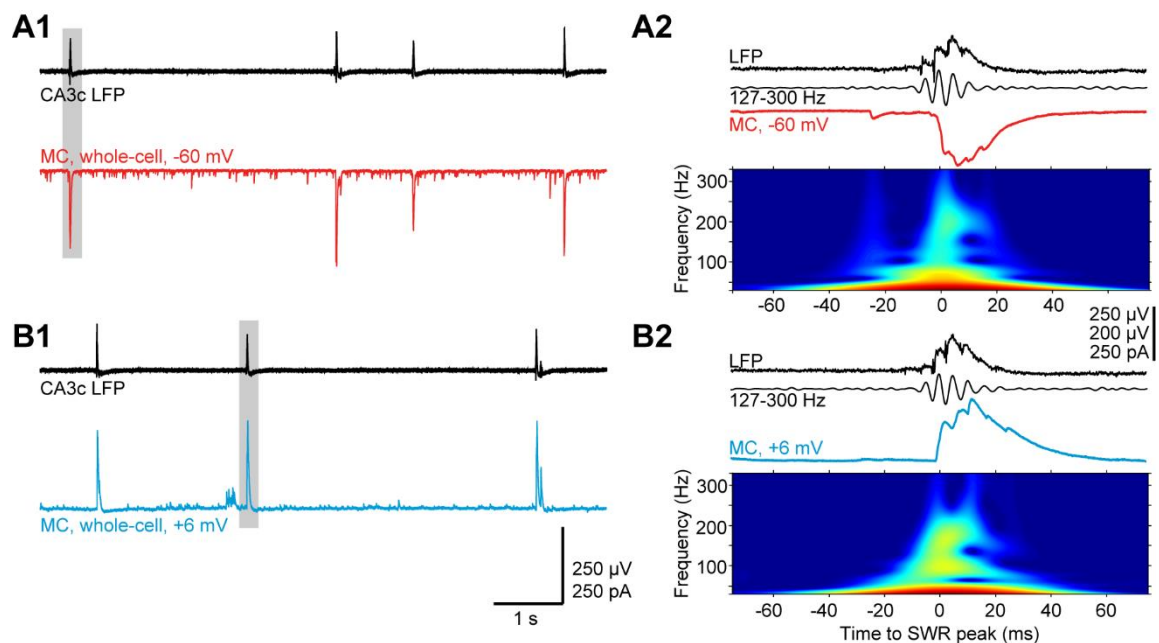

Figure 4: SWR-associated synaptic inputs in MCs. A1,B1. SWRs in CA3c (*top*) linked with cEPSCs and cIPSCs in MCs (*red* and *blue*). **A2,B2.** Events marked in *A* at higher resolution; *top to bottom:* LFP SWR, filtered version, and cEPSC (*red*) and cIPSC (*blue*). *Below*: Wavelet spectrograms of the cEPSC and cIPSC, warmer colours represent higher power.

The reversal of these SWR-linked cPSCs was calculated by extrapolating cPSC charge transfer values from different holding potentials -70, -60, -50 and -40 mV (with K gluconate-based intracellular solution) and was found to be -41.2mV (Fig. 5).
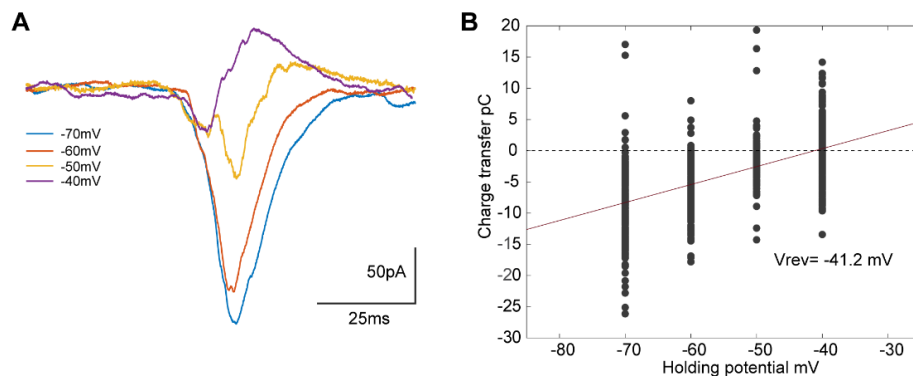

Figure 5: Reversal potential of SWR-associated currents in MCs. A. Representative mean SWR-associated currents at different holding potentials from a MC. **B.** Plot of charge transfer (pC) (*n*=12) determined at different holding potentials to calculate the potential of reversal of SWR-associated currents.

The phases of cEPSCs and cIPSCs, determined using a derivative peak time method (Fig. 6A), were found to be clustered with respect to the CA3 ripple (*P*<1×10^{-8} and *P*<9×10^{-7}, Rayleigh test; Fig. 6B). Comparison of the resultant phases showed a lead of excitatory over inhibitory synaptic inputs (cEPSC- and cIPSC-to-ripple phase: 14.3°±8.2°, vector strength 0.29 *vs* 39.2°±9.9°, vector strength 0.26). To disentangle the individual ripple-related synaptic inputs along the temporal dimension, the time points or the absolute amplitude of 10% steepest slopes of each ripple-related input was plotted against time in a 2-D histogram (See *Materials and Methods*). The input- and amplitude-time histograms of excitatory and inhibitory cPSCs revealed a rhythmic occurrence (peaks at intervals ~5ms); with strongest cluster of inputs occurring close to the LFP ripple peak (0 represents the peak of the LFP ripple; Fig. 6C-D).

11
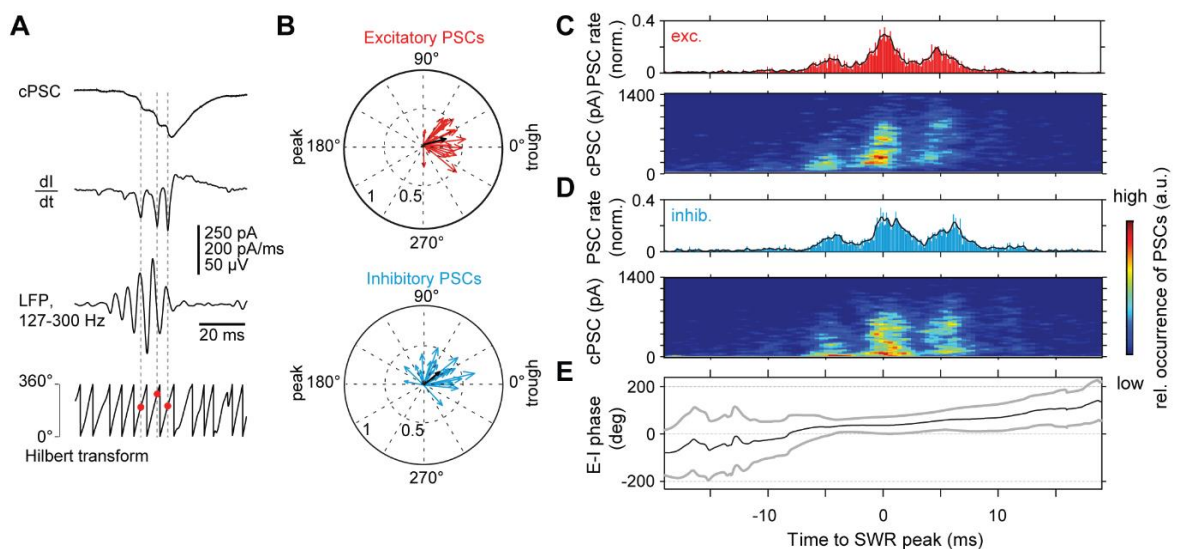
Figure 6: Analysis of cPSC-to-ripple phases. A. *Top:* Time points of steepest rising slopes in cPSC identified by their first derivatives (*middle*). The phases of these time points were determined with respect to the ripple (LFP) using its Hilbert phase (red dots, *bottom*). **B.** Polar plots of average phases of excitatory (*red*) and inhibitory (*blue*) PSCs of each cell with respect to CA3 ripples, *black arrows*: resultant phase vectors. **C-D.** *Upper*: Histograms of the time points of the strongest 10% slopes of synaptic inputs, for excitatory (*C, n=2770*) and inhibitory (*D, n=3012*) cPSCs. *Lower*: corresponding amplitude-time histograms **E.** Temporal evolution of cEPSC-to-cIPSC phase difference.

The temporal relation between excitatory and inhibitory inputs was analyzed by comparing the phase difference between cEPSCs and cIPSCs. The phase difference uncovers that the cIPSCs were almost phase-locked with the cEPSCs in the initial phase of the SWR event but start to lag increasingly behind the cEPSCs after the peak of the ripple phase (Fig. 6E). This phase shift in SWR-coupled excitation and inhibition could likely explain the spiking of cells in the period after the maximum of ripple peak (Fig. 3H). In addition, current clamp recordings revealed ripple-coherent EPSPs in MCs during CA3 SWRs (Fig. 7), indicating that SWR-related excitatory inputs result in EPSPs leading to APs in MCs.
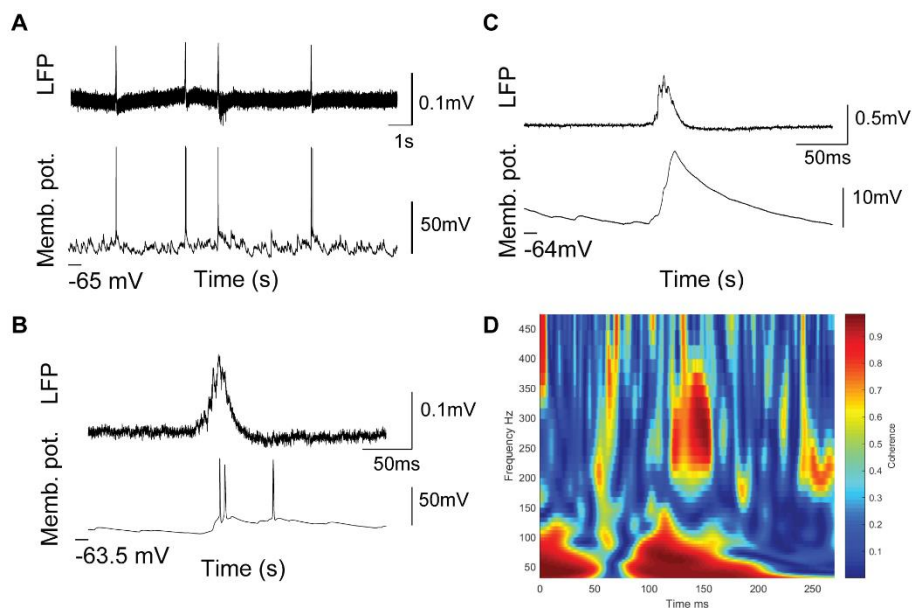

Figure 7: Membrane potential changes in MCs during SWRs. A. Representative trace of CA3 SWRs and corresponding current-clamp recording from a responding MC. **B.** Magnification of the marked event from A showing APs in MC. **C.** EPSPs in a non-responding MC during SWR event. **D.** Time-frequency-coherence plot of the mean LFP and the corresponding mean EPSP in a non-responding MC (*n=59* sweeps, same as C). Note the strong coherence of EPSP with respect to the LFP in the ripple frequency range.

To quantify the propagation time of SWR-related synaptic activity to MCs, we performed cross-correlation analyses of cPSCs with CA3 SWRs. Consistent with the monosynaptic delays reported by Scharfman (1994), we found time lags of ~5 ms for cEPSCs (mean: 4.8±0.3 ms, median: 4.9 ms; 1214 events; Fig. 8A1), while time lags for cIPSCs were prolonged (mean: 5.9±0.4 ms,

median: 5.7 ms, 1187 events; *P*=0.0005, paired two-tailed *t*-test, *n*=25 cells; Fig. 8A2). We then performed simultaneous recordings from PCs and MCs with the CA3 LFP to confirm the LFP-cPSC propagation delays with CA3 cPSC- MC cPSC latencies. Figure 7B displays the ripple-triggered averages of SWRs and corresponding cEPSCs and cIPSCs in both, a PC and an MC (green and orange; reconstructions, Fig. 8C). We found consistently delayed cPSCs in MCs compared with PCs (cEPSC delays: mean: 3.8±0.5 ms, median: 3.6 ms; cIPSC delays: mean: 5.9±0.7 ms, median: 5.7 ms; *n*=15). Moreover, inhibitory latencies were prolonged, compared to excitatory latencies (*P*=0.006, paired two-tailed *t*-test, Fig. 8D). These findings confirm a reliable and delayed propagation of CA3 ripple-related synaptic activity to MCs.
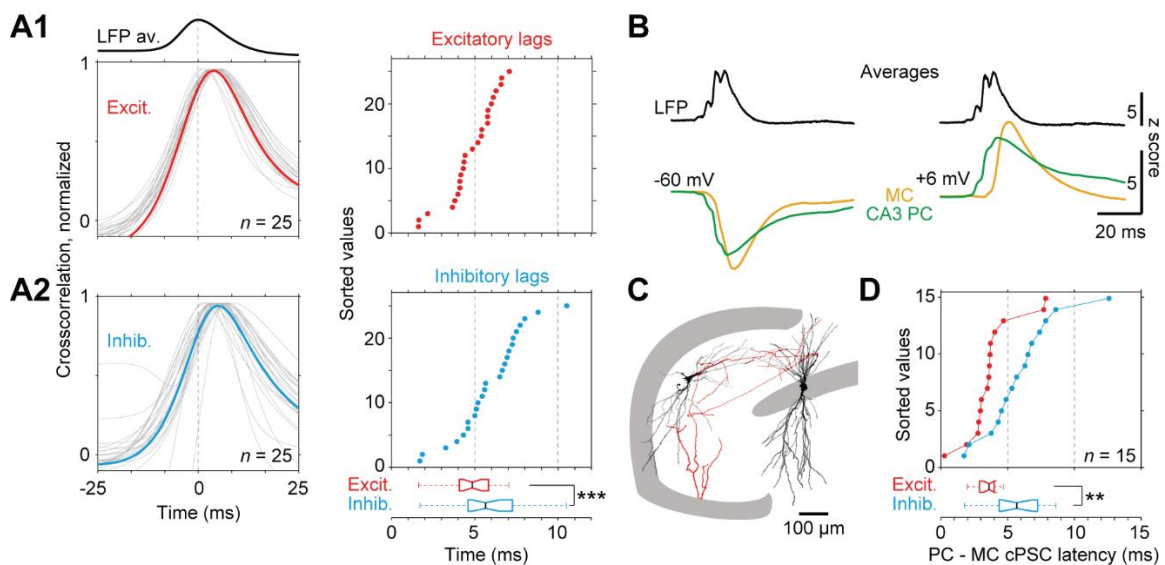

Figure 8: Timing of SWR-linked synaptic inputs in MCs. A. Crosscorrelation (CC) of LFP-cEPSCs (*Left*, **A1**) and LFP-cIPSCs (**A2**); single (*grey*) and averaged (*red* and *blue*) CC functions, aligned to peak of SPW envelope (*top*). *Right:* Median SPW-cPSC time lags for cEPSCs (*red*) and cIPSCs (*blue*). *Bottom*: cIPSCs are delayed compared to cEPSCs. **B.** Ripple peak-triggered averages of 100 SWRs (*top*) and their excitatory (*left*) and inhibitory (*right*) cPSCs in simultaneous PC-MC recordings (PC *green*, MC *orange*) **C.** Reconstructions of a CA3 PC and a MC **D.** Median latencies for cEPSCs (*red*) and cIPSCs (*blue*). Inhibitory latencies, compared to excitatory latencies, are consistently delayed in simultaneously recorded PCs and MCs (*bottom*).

5.3 Comparison of SWR-related synaptic inputs in mossy cells and CA3 pyramidal cells

To gain insights into the factors accounting for the higher fraction of MCs recruited during SWRs compared with the neighbouring CA3 PCs, we asked whether there are differences in the excitatory to inhibitory charge transfer (E/I) ratio of SWR-related inputs or intrinsic properties between MCs and CA3 PCs. We recorded cEPSCs and cIPSCs from both MCs and CA3c PCs at -60mV and +6mV respectively with the field in the CA3c area (Fig. 9A-B). Figure 9C represents the average LFP and the corresponding cEPSC/cIPSC in PC (*green*) and MC (*orange*). The excitatory or

inhibitory charge transfer values were calculated by integrating the cPSCs with varying time windows computed for each event. The E/I ratio was then calculated by dividing the excitatory to the inhibitory charge transfer values. The SWR-associated excitation and inhibition in CA3c PCs was larger compared to that of the MCs (MC *vs* CA3 PC- Excitation: -10.2 ± 2 pC *vs* -21.7 ± 3 pC, *P*=0.007, two-tailed unpaired *t*-test; Inhibition: 10.8 ± 2 pC *vs* 34.5 ± 4 pC, *P*=0.0003, two-tailed unpaired *t*-test; Fig. 9D). However, the E/I ratio was larger in MCs compared to CA3c pyramidal cells (mean: -1.36 ± 0.3 *vs* -0.65 ± 0.1, *P* = 0.04, two-tailed unpaired *t*-test; Fig. 9E), revealing a bias towards excitation in MCs. The input resistance of MCs was also larger compared to that of CA3 PCs (mean: 312.8 ± 31 MΩ *vs* 192.7 ± 35 MΩ Mann-Whitney *U*-Test, *P*=0.02; Fig. 9F; also shown by Scharfman and Schwartzkroin, 1988). Taken together, these factors might account for higher likelihood of SWR-linked spiking in MCs compared to CA3 PCs.
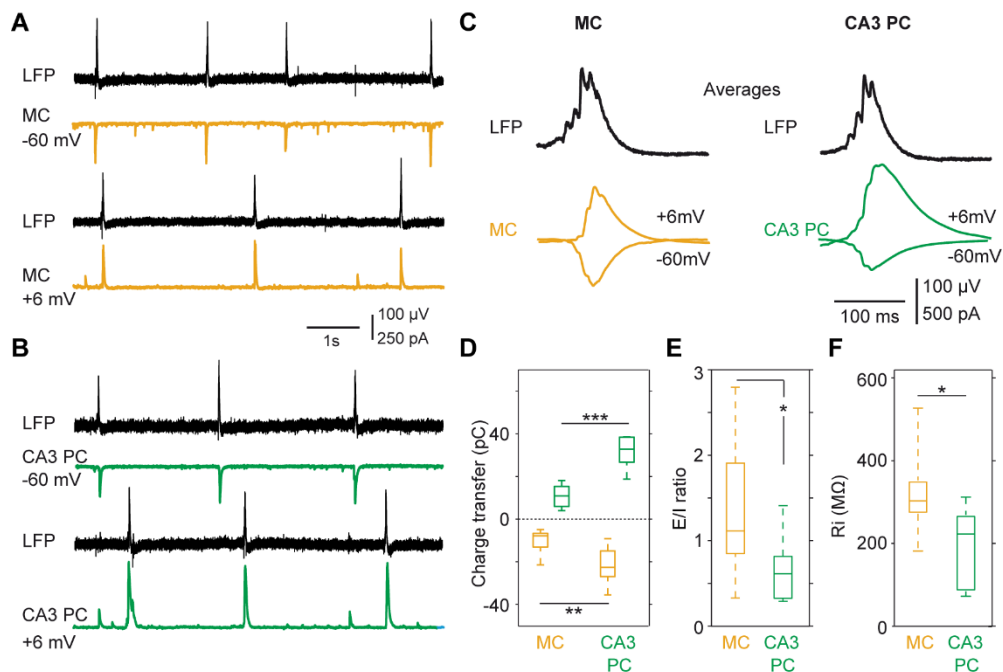

Figure 9: Comparison of SWR-associated excitatory and inhibitory synaptic inputs in MCs and CA3 PCs. An example LFP recording from CA3c (*green*) together with excitatory cPSCs and inhibitory PSCs in MC (*orange*) (**A**) and CA3 PC (**B**) recorded sequentially in the same slice. **C.** Ripple-triggered average cEPSC and cIPSC in MC and CA3 PC with the CA3 SWR. **D.** Comparison of charge transfer values of SWR-linked EPSCs and IPSCs in MCs and CA3 PCs shows stronger inhibition in CA3 PCs than in MCs. **E.** Excitatory to inhibitory charge transfer ratios in MCs and CA3 PCs. **F.** Comparison of input resistance in MCs and CA3 PCs as calculated from 100 sweeps of -4mV voltage deflections.

5.4 SWR-linked excitatory synaptic activity is routed to granule cells *via* mossy cells

Since the major output of mossy cells is onto the granule cells (Scharfman, 1995), we investigated whether the activation of MCs during SWRs has influence on the GCs. Indeed, GCs received

SWR-associated excitatory synaptic inputs but displayed a high variability in the occurrence of inputs compared to MCs (Fig. 10A,C). We therefore sought to quantify statistically whether a given cell received synaptic input causally linked to CA3 SWRs. The SWR-associated cEPSCs were quantified by comparing the amplitudes of SWR-related bins to the outside SWR-related bins (20ms) using one-way repeated measures ANOVA (Fig. 10A, *bottom*). We found 19 out of 29 GCs, *i.e*, 66% received significant SWR-associated cEPSCs (P < 0.0001) with mean failure rate of 49%. The low reliability of cEPSCs is suggestive of either a failure of transmission at the MC→GC synapse or local inhibition of GCs (Scharfman, 1995). In a subset of experiments, we recorded SWR-linked inhibitory synaptic currents in GCs. We found 13 out of 22, *i.e*, 60% GCs show significant cIPSCs (P < 0.0001) with mean failure rate of 66% (Fig. 10B).
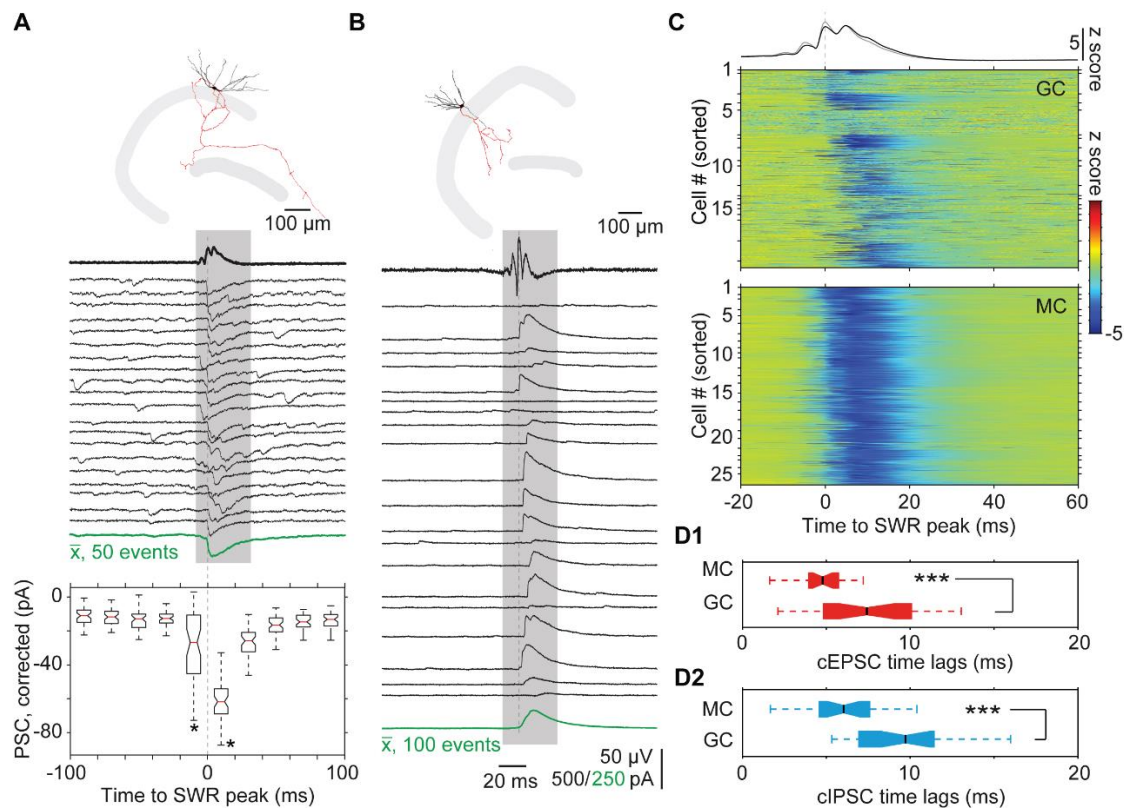
Figure 10: SWR-related synaptic activity in DG GCs and comparison to MCs. A and B. Synaptic activity in GCs during CA3 SWRs. *Top row:* reconstructed GCs. **A.** 20 successive sweeps of cEPSCs in GCs centered on the peak of CA3 SWRs. *Green trace:* average of 50 sweeps. *Bottom:* boxplot representation of cEPSC amplitudes in 20 ms time bins of all 50 sweeps. **B.** 20 successive sweeps of cIPSCs in GCs centered on the peak of CA3 SWRs. *Green trace:* average of 100 cIPSCs. **C.** Colour plots of individual z-scored SWR-linked baseline-corrected cEPSCs in GCs (*above, n = 19*) and MCs (*below, n = 25*) displayed from -20 ms to +60 ms with respect to the SWR peak (*top:* z-scored grand averages of CA3 SWRs (black and grey)). The colour bar (*right*) represents the z-scored amplitude values. **D1.** Comparison of median LFP-cEPSC median time lags. **D2.** Comparison of LFP-to-cIPSC median time lags.

Having observed SWR-related cEPSCs, we next investigated the timing of cEPSCs in GCs. The cross-correlation based LFP-cEPSC time lags in GCs were delayed compared to MCs (9.8 ± 1.04 ms vs 4.8 ± 0.3 ms; GC vs MC; Fig. 10D1). The LFP-cIPSC time lags based on cross correlation revealed a more complex SWR-mediated inhibition involving more than one synapse (9.4 ± 9.2 ms vs 5.9 ± 0.4 ms; GC vs MC; Fig. 10D2). The excitatory time lags were further substantiated by comparison of cEPSC timings from simultaneously recorded GCs and MCs (Fig. 11A1-2). We found that SWR-related cEPSCs in GCs consistently lagged behind those detected in MCs, with an average delay of 4.2 ± 0.6 ms (median: 4.1 ms, n=16 cells, Fig. 11B,C), implying a propagation of SWR-related activity from CA3 to DG via MCs. This hypothesis was strengthened by applying a different approach: based on the anatomical projections (CA3→MC→GC) and the high failure rates at the MC→GC synapse (22% on average; Scharfman, 1995), we reasoned that the cEPSCs in MCs might be more tightly coupled with CA3 SWRs than those in GCs. We, therefore, correlated individual CA3 SWR amplitudes with the corresponding cEPSC amplitudes in CA3 PCs (31 slices), MCs (56 slices) and GCs (38 slices). The medians of the distributions are similar for PCs and MCs (0.58 vs 0.56, red lines), but considerably lower for GCs (0.18). We obtained transformed Fisher's Z values to statistically compare these data and found no difference for Z values representing LFP–PC and LFP–MC correlations (P=0.94, Tukey's multiple comparisons test), while Z values representing LFP–GC correlations were significantly smaller (P<0.0001 for both comparisons, Tukey's multiple comparisons test; Fig. 11D).
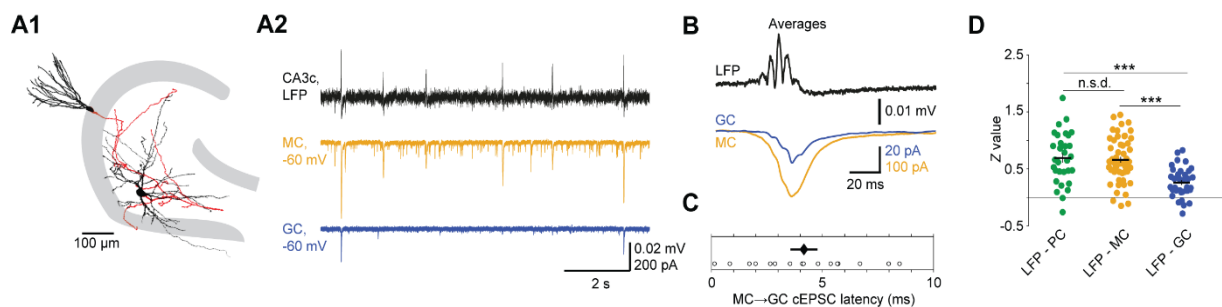
Figure 11: Ripple-associated functional coupling of CA3 and GCs *via* MCs. A1. Reconstruction of simultaneously recorded MC and GC. **A2.** Example sweeps, same experiment as *A1*. *Top:* CA3 SWR and corresponding cEPSCs in MC (*orange*) and GC (*blue*). **B** Ripple peak-triggered average of 100 SWRs (*top*) and corresponding cEPSCs (as *A1-2*). **C.** Median latencies (16 MC-GC recordings; *diamond*, average). **D.** Correlation of CA3c SWR and cEPSC amplitudes in PCs, MCs and GCs. Comparison of Fisher's Z values. Dots, Z-transformed correlation coefficients from the histograms in *C*.

Together, these results demonstrate an *indirect* propagation of SWR-related excitatory activity from CA3 PCs onto GCs *via* MCs.

6. Discussion

Until now, the role of mossy cells in the dentate gyrus- CA3 network during SWRs has not been explored in detail and could shed light on the DG-CA3 interactions during SWRs. The low density of MCs deep in the hilus (~10,000 MCs in the rat; Henze and Buzsáki, 2007; Myers and Scharfman, 2009) and their particular sensitivity to excitotoxicity (Ratzliff et al., 2002; Scharfman, 2016) pose a technical challenge for studying their behavior during different brain states (Scharfman and Myers, 2012; GoodSmith et al., 2017). In the present study, we used an *in vitro* slice model of SWRs to study MCs in a targeted way. We find that a significant fraction of MCs are recruited during spontaneous SWRs *in vitro*, with spiking delayed with respect to the CA3 ripple peak. The results of our study corroborate with recent studies *in vivo* in behaving rodents showing that the MCs are more active during the NREM state than wake or REM states (Senzai and Buzsaki, 2017; Goodsmith *et al* 2017).

Underlying the spiking, we observed prominent, reliable and ripple-coherent SWR-associated excitatory synaptic inputs in MCs, implying a functional coupling between CA3c area and MCs during SWRs. This functional coupling is in line with the excitatory monosynaptic back-projection from CA3 pyramidal neurons onto MCs (Scharfman, 1994). The cross-correlation based CA3 LFP-cEPSC time lags in MCs were prolonged, which was validated by cEPSC latencies in MCs determined from simultaneous CA3 PC-MC recordings. These latencies were comparable to the CA3-MC unitary connections shown previously by Scharfman. In addition, EPSC amplitudes were significantly correlated to the SWR amplitudes suggesting a direct influence of active CA3c pyramidal cells on the excitation of MCs.

Similar to excitation, we also observed prominent and ripple-coherent SWR-associated inhibitory synaptic inputs in MCs. The cross-correlation based LFP -cIPSC time lags were prolonged compared to those of excitatory cPSCs, further validated by latencies determined in simultaneous cIPSC recordings from PCs and MCs. Moreover, in contrast to the excitation, the IPSC amplitudes were not correlated to the SWR amplitudes implying a more complex inhibition in place. The possible sources of SWR-associated inhibition in MCs could arise directly from the CA3 interneurons such as basket, bistratified, O-LM interneurons, known to be active during SWRs (Lasztóczi et al., 2011; Hájos et al., 2013; Tukker et al., 2013), or CA1/CA3 boundary- crossing interneurons (Szabo et al., 2017) or mossy-fiber associated interneurons (Vida and Frotscher, 2000) projecting to the DG or indirectly through disynaptic inhibition by hilar interneurons

targeted by CA3 pyramidal cells (Sík et al., 1997; Hosp et al., 2014). A direct inhibition seems to be more likely, given the reliable and rhythmic occurrence of cIPSCs in MCs.

The observation that a significant fraction of MCs are active during SWRs is in stark contrast to only a small fraction of the neighbouring CA3 pyramidal cells active *in vitro* (Hajos et al., 2013). Are these two neuron populations different in their intrinsic properties or network excitability? Our data reveal a higher E/I ratio of SWR-associated inputs and higher input resistance in MCs compared to CA3 pyramidal cells, increasing the propensity of MCs to spike during SWRs (see also, Scharfman and Schwartzkroin, 1988). Another characteristic feature of MCs is the spontaneous barrage of excitatory synaptic activity at rates higher than in CA3 PCs (Scharfman and Schwartzkroin, 1988; Strowbridge et al., 1992), making the MCs more excitable.

The main target of the mossy cells are the dentate granule cells in ipsilateral and contralateral DG and hilar interneurons (Scharfman, 1995, 1996, Larimer and Strowbridge, 2008, Berger et al., 1981; Ribak et al., 1985; Hsu et al., 2016). What could be the consequences of MC spiking in the DG network? Dentate GCs have been shown to be active during SWRs (Buzsáki, 1986; Ylinen et al., 1995; Hulse et al., 2017) and slow wave sleep (SWS, Senzai and Buzsáki, 2017). We speculated whether SWR activity in CA3 could propagate to the DG via active MCs. We indeed found that ~66% of the recorded GCs receive significant SWR-associated excitatory synaptic inputs. The LFP-cEPSC latencies in GCs were consistently delayed compared to those of simultaneously recorded MCs, indicating a disynaptic excitatory chain from CA3 pyramidal cells to granule cells mediated by MCs. This is further supported by strong correlations between CA3 SWR amplitudes and cEPSC amplitudes in both PCs and MCs, but not in GCs, demonstrating a direct coupling of the CA3 PCs and MCs, but not GCs.

MCs are located in a strategic position in the dentate-hilar-CA3 network, enabling them to integrate information from GCs and CA3 PCs and project both ipsilaterally and contralaterally to the inner molecular layer of DG. What functional role could the MCs play in the network? In the context of spatial processing, recent findings show multiple place fields and pronounced remapping in MCs compared to GCs, leading to the hypothesis that MCs might receive spatial information from CA3 PCs (Senzai and Buzsaki, 2017; Danielson et al., 2017). In addition, the current study and several *in vivo* studies demonstrate that MCs have high firing rates during SWRs and SWS. It has been proposed by Lisman (1999) that the feedback information from CA3 routed to DG by MCs could enable error correction, which is important for accurate sequential memory recall.

18

How could the MCs mediate such function in the DG network? There is evidence showing the net effect of MC projection onto GCs is inhibition (Buzsaki and Czeh, 1981; Hsu et al., 2016; Scharfman 1995, 2016). However, because of the wide extent of septo-temporal connectivity to GCs (Buckmaster et al., 1996), MCs have, therefore, been speculated to activate spatially distinct sparse subsets of granule cells by feedback excitation, possibly from CA3, and simultaneously suppress other granule cells via local hilar interneurons (Soltesz et al., 1993; Henze 2007; Scharfman, 2013; Senzai and Buzsaki, 2017). These features place MCs as a neuronal hub linking local and distal compartments of both hippocampi. One could, therefore, speculate that in the context of hippocampal oscillations, MCs might be involved in synchronizing neuronal assemblies along the septo-temporal axis and between the two hippocampi during different brain states. Indeed, it has been shown that the theta coherence during REM sleep is higher between hemispheres than within a hemisphere and CA3/mossy projections to contralateral hemisphere are thought to be a major determinant underlying this coherence (Sabolek et al., 2009). Elucidating the function of mossy cells in the DG-hilar-CA3 network is thus crucial for understanding normal hippocampal functions and also during diseased states such as epilepsy and psychiatric disorders (Scharfman, 2016).

Conclusion and Outlook

In conclusion, our results provide a first description of the involvement of mossy cells during SWRs and suggest a major role for these cells in the SWR-related hippocampal functions and memory consolidation process. In the next steps, we hope to expand the current knowledge to understand the ripple-related function of mossy cells and address these questions:

1. What are the functions of mossy cells during SWRs *in vivo*?

2. How are mossy cells involved in encoding spatial information?

3. What is the role of neuromodulators in influencing mossy cell activity?

We hope our study will form basis for future research on mossy cell/hilar function in different brain rhythms during physiological and pathophysiological states.

7. References

Acsády, L., Katona, I., Martínez-Guijarro, F.J., Buzsáki, G., Freund, T.F. (2000) Unusual target selectivity of perisomatic inhibitory cells in the hilar region of the rat hippocampus. J Neurosci *20*:6907–19.

Amaral, D.G. (1978) A Golgi study of cell types in the hilar region of the hippocampus in the rat. J Comp Neurol *182*:851–914.

Berens, P. (2009) CircStat: A MATLAB toolbox for circular statistics. J Stat Softw *31*:1–21.

Berger, T.W., Semple-Rowland, S., Bassett, J.L. (1981) Hippocampal polymorph neurons are the cells of origin for ipsilateral association and commissural afferents to the dentate gyrus. Brain Res *215*:329–36.

Bortz, J., Schuster, C. (2010) Statistik für Human- und Sozialwissenschaftler. 7 Auflage. (Berlin-Heidelberg, Germany: Springer-Verlag).

Buckmaster, P.S., Strowbridge, B.W., Schwartzkroin, P.A. (1993) A comparison of rat hippocampal mossy cells and CA3c pyramidal cells. J Neurophysiol *70*:1281–99.

Buckmaster, P.S., Wenzel, H.J., Kunkel, D.D., Schwartzkroin, P.A. (1996) Axon arbors and synaptic connections of hippocampal mossy cells in the rat in vivo. J Comp Neurol *366*:270–92.

Buzsáki, G. and Eidelberg, E. (1981) Commissural projection to the dentate gyrus of the rat: evidence for feed-forward inhibition. Brain Res *230*, 346–50.

Buzsáki, G. (1986) Hippocampal sharp waves: Their origin and significance. Brain Res *398*:242–52.

Buzsáki, G., Buhl, D.L., Harris, K.D., Csicsvari, J., Czéh, B., Morozov, A. (2003) Hippocampal network patterns of activity in the mouse. Neuroscience *116*:201–11.

Buzsáki, G. (2015) Hippocampal sharp wave-ripple: A cognitive biomarker for episodic memory and planning. Hippocampus *25*:1073–1188.

Cajal, R. (1911) Histologie du Systeme Nerveux de l'Homme et des Vertebretes, Vols. 1 and 2. A. Maloine. Paris.

Danielson, N.B., Turi, G.F., Ladow, M., Chavlis, S., Petrantonakis ,P.C., Poirazi, P., Losonczy, A. (2017) In Vivo Imaging of Dentate Gyrus Mossy Cells in Behaving Mice. Neuron *93*:552–9.

Frotscher, M., Seress, L., Schwerdtfeger, W.K., Buhl, E. (1991) The mossy cells of the fascia dentata: A comparative study of their fine structure and synaptic connections in rodents and primates. J Comp Neurol *312*:145–63.

Girardeau, G., Benchenane, K., Wiener, S.I., Buzsáki, G., Zugaro, M.B. (2009) Selective suppression of hippocampal ripples impairs spatial memory. Nat Neurosci *12*:1222–23.

GoodSmith, D., Chen, X., Wang, C., Kim, S.H., Song, H., Burgalossi, A., Christian, K.M,, Knierim, J.J. (2017) Spatial Representations of Granule Cells and Mossy Cells of the Dentate Gyrus. Neuron *93*:1–14.

Hájos, N., Karlócai, M.R., Németh, B., Ulbert, I., Monyer, H., Szabó, G., Erdélyi, F., Freund, T.F., Gulyás, A.I. (2013) Input-Output Features of Anatomically Identified CA3 Neurons during Hippocampal Sharp Wave/Ripple Oscillation In Vitro. J Neurosci *33*:11677–91.

Hashimotodani, Y., Nasrallah, K., Jensen, K.R., Chávez, A.E., Carrera, D., Castillo, P.E. (2017) LTP at Hilar Mossy Cell-Dentate Granule Cell Synapses Modulates Dentate Gyrus Output by Increasing Excitation/Inhibition Balance. Neuron *95*:928–43.

Henze, D.A., Buzsáki, G. (2007) Hilar mossy cells: functional identification and activity in vivo. Prog Brain Res *163*:199–217.

Henze, D.A., Urban, N.N., Barrionuevo, G. (2000) The multifarious hippocampal mossy fiber pathway: A review. Neuroscience *98*:407–27.

Hosp, J.A., Strüber, M., Yanagawa, Y., Obata, K., Vida, I., Jonas, P., Bartos, M. (2014) Morpho-physiological criteria divide dentate gyrus interneurons into classes. Hippocampus *24*:189–203.

Hsu, T.T., Lee, C.T., Tai, M.H., Lien, C.C. (2016) Differential Recruitment of Dentate Gyrus Interneuron Types by Commissural Versus Perforant Pathways. Cereb Cortex *26*:2715–27.

Hulse, B.K., Lubenov, E.V., Siapas, A.G. (2017) Brain State Dependence of Hippocampal Subthreshold Activity in Awake Mice. CellReports *18*:136–47.

Jinde, S., Zsiros, V., Jiang, Z., Nakao, K., Pickel, J., Kohno, K., Belforte, J.E., Nakazawa, K. (2012) Hilar Mossy Cell Degeneration Causes Transient Dentate Granule Cell Hyperexcitability and Impaired Pattern Separation. Neuron *76*:1189–1200.

Kowalski, J., Geuting, M., Paul, S., Dieni, S., Laurens, J., Zhao, S., Drakew, A., Haas, C.A., Frotscher, M., Vida, I. (2010) Proper layering is important for precisely timed activation of hippocampal mossy cells. Cereb Cortex *20*:2043–54.

Larimer, P., Strowbridge, B.W. (2008) Nonrandom Local Circuits in the Dentate Gyrus. J Neurosci *28*:12212–23.

Larimer, P. and Strowbridge, B. W. (2010) Representing information in cell assemblies: persistent activity mediated by semilunar granule cells. Nat. Neurosci. *13*, 213–222.

Lasztóczi, B., Tukker, J.J., Somogyi, P., Klausberger, T. (2011) Terminal field and firing selectivity of cholecystokinin- expressing interneurons in the hippocampal CA3 area. J Neurosci 31:18073–93.

Lee, A.K., Wilson, M.A. (2002) Memory of sequential experience in the hippocampus during slow wave sleep. Neuron *36*:1183–94.

Leutgeb, J.K., Leutgeb, S., Moser, M.B., and Moser, E.I. (2007). Pattern separation in the dentate gyrus and CA3 of the hippocampus. Science *315*, 961–966.

Li, X.G., Somogyi, P., Ylinen, A., Buzsáki, G. (1994) The hippocampal CA3 network: An in vivo intracellular labeling study. J Comp Neurol *339*:181–208.

Lisman, J.E. (1999) Relating hippocampal circuitry to function: recall of memory sequences by reciprocal dentate-CA3 interactions. Neuron *22*:233–42.

Lorente de Nó, R. (1934) Studies on the Structure of the Cerebral Cortex. II. Continuation of the Study of the Ammonic System. J für Psychol und Neurol *46*:113–77.

Margerison, J. & Corsellis, J. (1966) Epilepsy and the temporal lobes: a clinical, electrographic and neuropathological study of the brain in epilepsy with particular reference to the temporal lobes. Brain *89*, 499–530.

Maier, N., Morris, G., Johenning, F.W., Schmitz, D. (2009) An approach for reliably investigating hippocampal sharp wave-ripples in vitro. PLoS One 4:1–10.

Maier, N. and Kempter, R. (2017). Hippocampal Sharp Wave/Ripple Complexes—Physiology and Mechanisms. In Cognitive Neuroscience of Memory Development, N. Axmacher and B. Rasch, eds. (Switzerland: Springer International Publishing), pp. 227–49.

Myers, C.E., and Scharfman, H.E. (2009) A Role for hilar cells in pattern separation in the dentate gyrus: A computational approach. Hippocampus *19*:321–37.

Neunuebel, J.P., Knierim, J.J. (2012) Spatial Firing Correlates of Physiologically Distinct Cell Types of the Rat Dentate Gyrus. J Neurosci *32*:3848–58.

Ólafsdóttir, F.H., Bush, D. and Barry, C. (2018) The Role of Hippocampal Replay in Memory and Planning. Current Biology *28*, R37–R50.

Patel, J., Schomburg, E.W., Berényi, A., Fujisawa S, Buzsáki G (2013) Local generation and propagation of ripples along the septotemporal axis of the hippocampus. J Neurosci *33*:17029–41.

Ratzliff, A., Santhakumar, V., Howard, A. & Soltesz, I. (2002) Mossy cells in epilepsy: rigor mortis or vigor mortis? Trends Neurosci. *25*, 140–144.

Ribak, C.E., Seress, L., Amaral, D.G. (1985) The development, ultrastructure and synaptic connections of the mossy cells of the dentate gyrus. J Neurocytol *14*:835–57.

Sabolek, H.R., Penley, S.C., Hinman, J.R., Bunce, J.G., Markus, E.J., Escabi, M., Chrobak, J.J. (2009) Theta and gamma coherence along the septotemporal axis of the hippocampus. J Neurophysiol. *101*(3):1192-200.

Scharfman, H.E., and Schwartzkroin, P.A. (1988) Electrophysiology of morphologically identified mossy cells of the dentate hilus recorded in guinea pig hippocampal slices. J Neurosci *8*:3812–21.

Scharfman, H.E., Kunkel, D.D., Schwartzkroin, P.A. (1990) Synaptic connections of dentate granule cells and hilar neurons: Results of paired intracellular recordings and intracellular horseradish peroxidase injections. Neuroscience *37*:693–707.

Scharfman, H. E. (1991) Dentate hilar cells with dendrites in the molecular layer have lower thresholds for synaptic activation by perforant path than granule cells. J. Neurosci. *11*, 1660–1673.

Scharfman, H.E. (1994) Evidence from simultaneous intracellular recordings in rat hippocampal slices that area CA3 pyramidal cells innervate dentate hilar mossy cells. J Neurophysiol *72*:2167–80.

Scharfman, H.E. (1995) Electrophysiological evidence that dentate hilar mossy cells are excitatory and innervate both granule cells and interneurons. *74*:179–94.

Scharfman, H.E. (1996) Conditions required for polysynaptic excitation of dentate granule cells by area CA3 pyramidal cells in rat hippocampal slices. Neuroscience *72*:655–68.

Scharfman, H.E., and Myers, C.E. (2012) Hilar mossy cells of the dentate gyrus: a historical perspective. Front Neural Circuits *6*:106.

Scharfman, H.E. (2016) The enigmatic mossy cell of the dentate gyrus. Nat Rev Neurosci *17*:562–75.

Senzai, Y., Buzsáki, G. (2017) Physiological properties and behavioral correlates of hippocampal granule cells and mossy cells. Neuron: *93*:691-704.

Sík, A., Penttonen, M., Buzsáki, G. (1997) Interneurons in the hippocampal dentate gyrus: An in vivo intracellular study. Eur J Neurosci *9*:573–88.

Soltesz, I., Bourassa, J. & Deschenes, M. (1993) The behavior of mossy cells of the rat dentate gyrus during theta oscillations *in vivo*. Neuroscience *57*, 555–564.

Soriano, E, Frotscher, M. (1994) Mossy cells of the rat fascia dentata are glutamate-immunoreactive. Hippocampus *4*:65-9.

Strowbridge, B.W., Buckmaster, P.S., Schwartzkroin, P.A. (1992) Potentiation of spontaneous synaptic activity in rat mossy cells. Neurosci Lett *142*:205–10.

Szabo, G.G., Du, X., Oijala, M., Varga, C., Parent, J.M., Soltesz, I. (2017) Extended interneuronal network of the dentate gyrus. Cell Rep *20*:1262-8.

Tukker, J.J., Lasztóczi, B., Katona, L., Roberts, J.D.B., Pissadaki, E.K., Dalezios, Y., Márton, L., Zhang, L., Klausberger, T., Somogyi, P. (2013) Distinct dendritic arborization and in vivo firing patterns of parvalbumin-expressing basket cells in the hippocampal area CA3. J Neurosci *33*:6809–25.

Vida, I., Frotscher, M. (2000) A hippocampal interneuron associated with the mossy fiber system. PNAS *97*(3):1275-80.

Williams, P. A., Larimer, P., Gao, Y. & Strowbridge, B. W. (2007) Semilunar granule cells: glutamatergic neurons in the rat dentate gyrus with axon collaterals in the inner molecular layer. J. Neurosci. *27*, 13756–13761.

Wilson, M.A., McNaughton, B.L. (1994) Reactivation of hippocampal ensemble memories during sleep. Science 29;265(5172):676-9.

Ylinen, A., Soltész, I., Bragin, A., Penttonen, M., Sík, A., Buzsáki, G. (1995) Intracellular correlates of hippocampal theta rhythm in identified pyramidal cells, granule cells, and basket cells. Hippocampus *5*:78–90.

8. Affidavit

I, Aarti Swaminathan, certify under penalty of perjury by my own signature that I have submitted the thesis on the topic 'Role of hilar mossy cells in the CA3-dentate gyrus network during sharp wave-ripple activity in vitro'. I wrote this thesis independently and without assistance from third parties, I used no other aids than the listed sources and resources.

All points based literally or in spirit on publications or presentations of other authors are, as such, in proper citations (see "uniform requirements for manuscripts (URM)" the ICMJE www.icmje.org) indicated. The section on methodology (in particular practical work, laboratory requirements, statistical processing) and results (in particular images, graphics and tables) corresponds to the URM (s.o) and are answered by me. My contribution in the selected publication for this dissertation corresponds to those that are specified in the following joint declaration with the responsible person and supervisor.

The importance of this affidavit and the criminal consequences of a false affidavit (section 156,161 of the Criminal Code) are known to me and I understand the rights and responsibilities stated therein.

_____

Date   Signature

9. Detailed Declaration of Contribution

Aarti Swaminathan had the following share in the following publication:

Publication: Swaminathan A, Wichert I, Schmitz D, Maier N. (2018) Involvement of Mossy Cells in Sharp Wave-Ripple Activity In Vitro. Cell Report, May 2018.

Contribution in detail:

Planning of the experiments:

Conception of the project by Schmitz D and Maier N, planning of the electrophysiology experiments was done by Swaminathan A, Maier N and Schmitz D

Execution of experiments:

Slicing and preparation of mouse hippocampal slices- Swaminathan A

Cell-attached/ on-cell and whole cell recordings from mossy cells- Swaminathan A (Fig. 1,2,3)

Simultaneous CA3-MC recordings- Swaminathan A, Maier N (Fig. 3)

Granule cell recordings- Swaminathan A, Maier N (Suppl. Fig. 4)

Simultaneous MC-GC recordings- Swaminathan A, Maier N (Fig. 4)

Immunostainings- Susanne Rieckmann (Fig. 1)

Confocal imaging, reconstructions in Fiji- Swaminathan A (Fig.1,3,4)

Data Analysis:

Intrinsic parameters, Spike time analysis, Cross-correlation analysis - Swaminathan A (Suppl Fig.1,2, Fig. 2,3)

Spectrogram, Input phase analysis- Ines Wichert (Fig. 3, Suppl. Fig.3)

Synaptic inputs in GCs, fidelity analysis- Swaminathan A and Maier N (Suppl. Fig.4)

CA3-MC and MC-GC latency analysis, Correlation analysis - Maier N (Fig.3,4)

Data visualisation: Maier N and Swaminathan A

Writing and editing of the manuscript: Maier N and Swaminathan A together with Wichert I and Schmitz D

Signature, date and stamp of the doctoral supervisor   Signature of the doctoral candidate

_____   _____

24

10. Publication

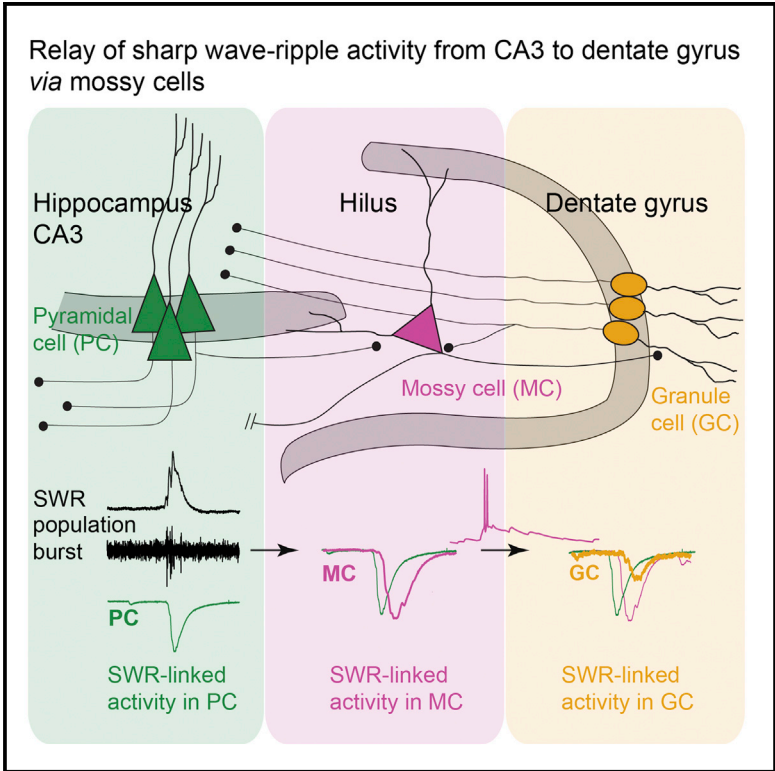Involvement of Mossy Cells in Sharp Wave-Ripple Activity In Vitro.

Swaminathan A, Wichert I, Schmitz D, Maier N. (2018)

Cell Reports 23(9):2541-2549.

Cell Reports

Involvement of Mossy Cells in Sharp Wave-Ripple Activity *In Vitro*

Graphical Abstract

Authors

Aarti Swaminathan, Ines Wichert,
Dietmar Schmitz, Nikolaus Maier

Correspondence

nikolaus.maier@charite.de

In Brief

The functional implication of hippocampal mossy cells (MCs) is thus far poorly understood. Swaminathan et al. demonstrate sub-threshold activity and recruitment of MCs during ripples that are fast neuronal oscillations involved in memory consolidation. These results suggest a pivotal role for MCs in computations occurring during ripple-related brain states.

Highlights

- Mossy cells (MCs) receive ripple-related excitatory and inhibitory synaptic inputs

- These inputs occur at high fidelity and are phase coherent with ripples

- Ripple-related synaptic activity can recruit MCs into the active network

- MC spiking can give rise to ripple-associated synaptic inputs in granule cells

CellPress

Report

Involvement of Mossy Cells
in Sharp Wave-Ripple Activity *In Vitro*

Aarti Swaminathan,[1,4] Ines Wichert,[2] Dietmar Schmitz,[1,2,3,4,5,6,7] and Nikolaus Maier[1,7,8,*]
[1]Charité-Universitätsmedizin Berlin, corporate member of Freie Universität Berlin, Humboldt-Universität zu Berlin, and Berlin Institute of Health, Neuroscience Research Center, 10117 Berlin, Germany
[2]Bernstein Center for Computational Neuroscience Berlin, 10115 Berlin, Germany
[3]Berlin Institute of Health, 10178 Berlin, Germany
[4]Cluster of Excellence NeuroCure, 10117 Berlin, Germany
[5]German Center for Neurodegenerative Diseases (DZNE) Berlin, 10117 Berlin, Germany
[6]Einstein Center for Neurosciences Berlin, 10117 Berlin, Germany
[7]Senior author
[8]Lead Contact
*Correspondence: nikolaus.maier@charite.de
https://doi.org/10.1016/j.celrep.2018.04.095

SUMMARY

The role of mossy cells (MCs) of the hippocampal dentate area has long remained mysterious. Recent research has begun to unveil their significance in spatial computation of the hippocampus. Here, we used an *in vitro* model of sharp wave-ripple complexes (SWRs), which contribute to hippocampal memory formation, to investigate MC involvement in this fundamental population activity. We find that a significant fraction of MCs (~47%) is recruited into the active neuronal network during SWRs in the CA3 area. Moreover, MCs receive pronounced, ripple-coherent, excitatory and inhibitory synaptic input. Finally, we find evidence for SWR-related synaptic activity in granule cells that is mediated by MCs. Given the widespread connectivity of MCs within and between hippocampi, our data suggest a role for MCs as a hub functionally coupling the CA3 and the DG during ripple-associated computations.

INTRODUCTION

The hippocampal dentate gyrus (DG) is considered the input structure where information from the entorhinal cortex is processed. The most abundant excitatory neurons in the DG, the granule cells (GCs), forward this input to the CA3 region via mossy fibers (Lorente de Nó, 1934; Henze et al., 2000). On their way to the CA3 area, mossy fibers contact the second population of glutamatergic cells in the DG, mossy cells (MCs), whose somata reside in the hilus (Amaral, 1978; Berger et al., 1981; Scharfman et al., 1990; Soriano and Frotscher, 1994). In addition to excitatory inputs from GCs, MCs receive inhibitory inputs from local interneurons and excitatory "back" projections from CA3 pyramidal cells (PCs) (Scharfman, 1994c; Acsády et al., 2000; Larimer and Strowbridge, 2008). The dendrites of MCs are

confined mostly to the hilus, but some extend to the molecular layer of the DG (Frotscher et al., 1991). MC axons ramify within the hilus and project to the inner molecular layers of both the ipsi- and the contralateral DG (Berger et al., 1981; Ribak et al., 1985; Buckmaster et al., 1996; Hsu et al., 2016). Taken together, these anatomical features suggest a strategic role for MCs in relaying information in the CA3-DG network, within and between hemispheres.

Recent studies have started to elucidate the activity of MCs across different behaviors (Neunuebel and Knierim, 2012; Danielson et al., 2017; GoodSmith et al., 2017). Specifically, MCs were shown to display higher firing rates during slow-wave sleep (SWS) compared with rapid eye movement (REM) sleep and alert behaviors (Senzai and Buzsáki, 2017). In the hippocampal electroencephalogram (EEG), SWS and quiet wakefulness are characterized by transient field events in the CA3 to CA1 regions, termed sharp waves, that occur in association with high-frequency (~120–250 Hz) ripple oscillations (sharp wave-ripple complexes [SWRs]; Buzsáki, 1986; for review see Buzsáki, 2015). During SWRs, neuron sequences previously active during behavior are re-activated, and this "replay" of activity is thought to support memory consolidation (Lee and Wilson, 2002; Girardeau et al., 2009; Jadhav et al., 2012).

The role of MCs in the context of SWRs remains unclear. Given the technical challenges of targeting MCs *in vivo*, a slice model of SWRs provides an attractive experimental system to investigate MCs during SWRs. Acute hippocampal slices can express sharp waves and ripples autonomously, in physiological bathing solutions, without drugs that elevate the network excitability (Maier et al., 2003, 2009, 2011; Both et al., 2008; Hájos et al., 2009, 2013; Papatheodoropoulos and Kostopoulos, 2002; Kubota et al., 2003; for review, see Maier and Kempter, 2017).

Here, we used this *in vitro* tool to elucidate MC activity during SWRs in acute slices of the mouse hippocampus. We identified SWR-associated synaptic currents in MCs and the recruitment of MCs into the active network. Taken together, our results suggest that SWR-associated information is relayed by MCs from CA3 "backward" into the network of the DG.
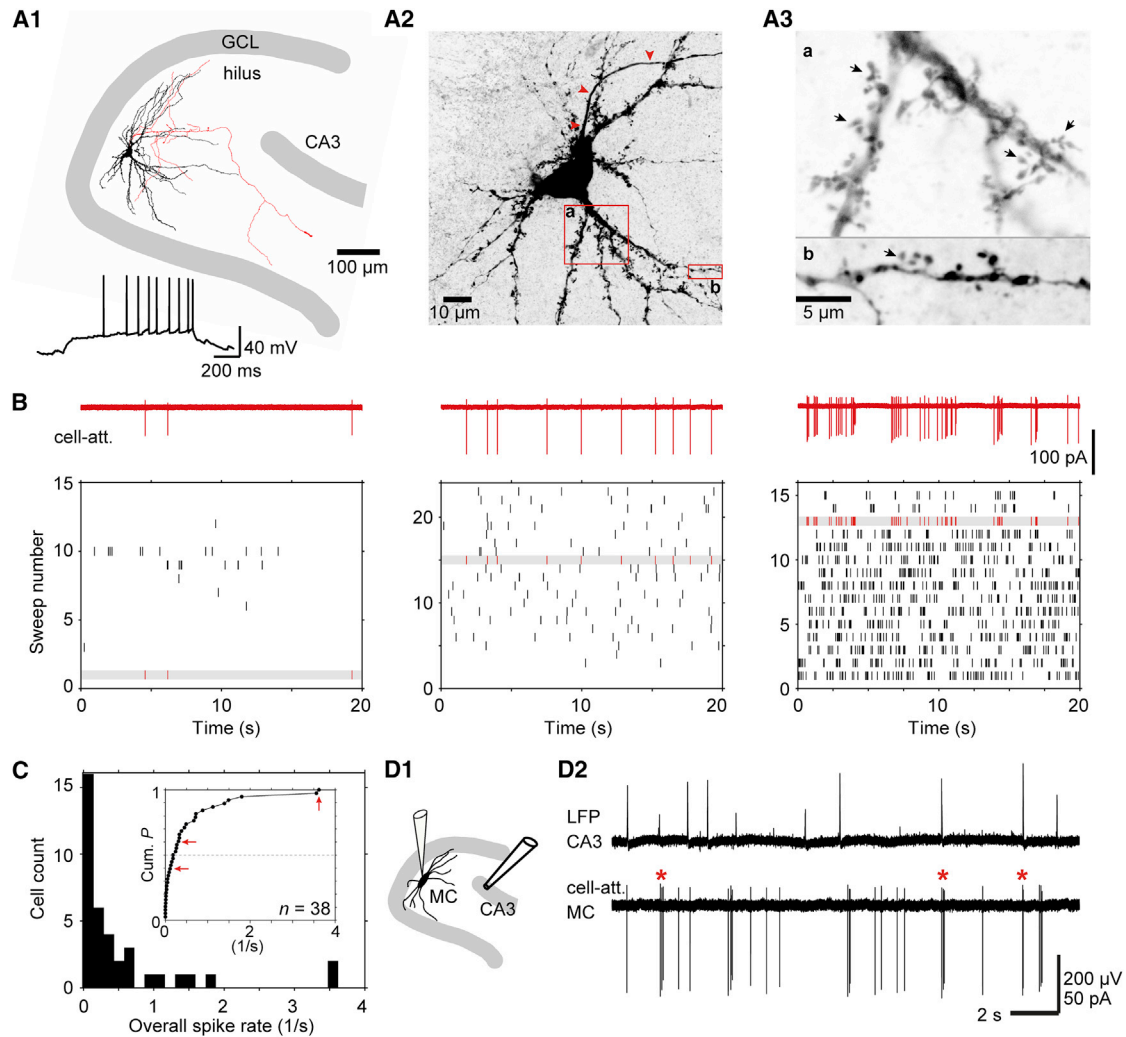
Figure 1. Spontaneous MC Activity in Mouse Hippocampal Slices
(A1) Reconstruction of a biocytin-filled MC. Dendrites in black, the axon in red. Below: the firing pattern during a 40 pA (1 s) current injection.
(A2) Confocal image showing complex spines on the proximal dendrites. Arrowheads mark the axon.
(A3) Magnification of the boxed areas in (A2) to visualize spines at higher resolution (arrows).
(B) Example recordings (top) and raster plots of successive sweeps show varied discharge behaviors in MCs.
(C) Histogram of overall spike rates. Inset: cumulative distribution of firing rates; red arrows indicate the cells shown in (B).
(D1) Sketch to illustrate parallel LFP-MC recordings.
(D2) Example showing the CA3 LFP and MC spiking. Asterisks indicate MC discharge concurrent with SWRs.

RESULTS

Properties of MCs

Across species and behavioral conditions, MCs have been shown to be a highly active class of hippocampal excitatory neurons (Henze and Buzsáki, 2007; GoodSmith et al., 2017; Senzai and Buzsáki, 2017). We used acute brain slices to study neuronal network mechanisms underlying MC activity. With differential interference contrast microscopy, we identified putative MCs as multipolar cells located in the hilus and outside the CA3c PC layer (Buckmaster et al., 1993; Figure 1A1). To identify MCs, all cells were biocytin labeled during recording and confirmed post hoc on the basis of morphological features. In particular, MCs exhibit a high density of large, complex spines ("thorny excrescences") on their proximal dendrites and soma (Figures 1A2 and 1A3; Amaral, 1978; Ribak et al., 1985). We used this property as a defining criterion, and consequently, only cells expressing thorny excrescences were included in our analysis. In addition, none of the included cells expressed the GABAergic marker GAD67 (Figure S1A). Stained axon collaterals of MCs were found in the hilus and the inner molecular layer, and often, cells displayed a major axon collateral extending toward the stratum oriens of CA3 (Figure 1A1; Amaral, 1978; Buckmaster et al., 1996). Electrophysiological properties of MCs are summarized in Figure S1B and were comparable with those of murine MCs reported by others (Kowalski et al., 2010).
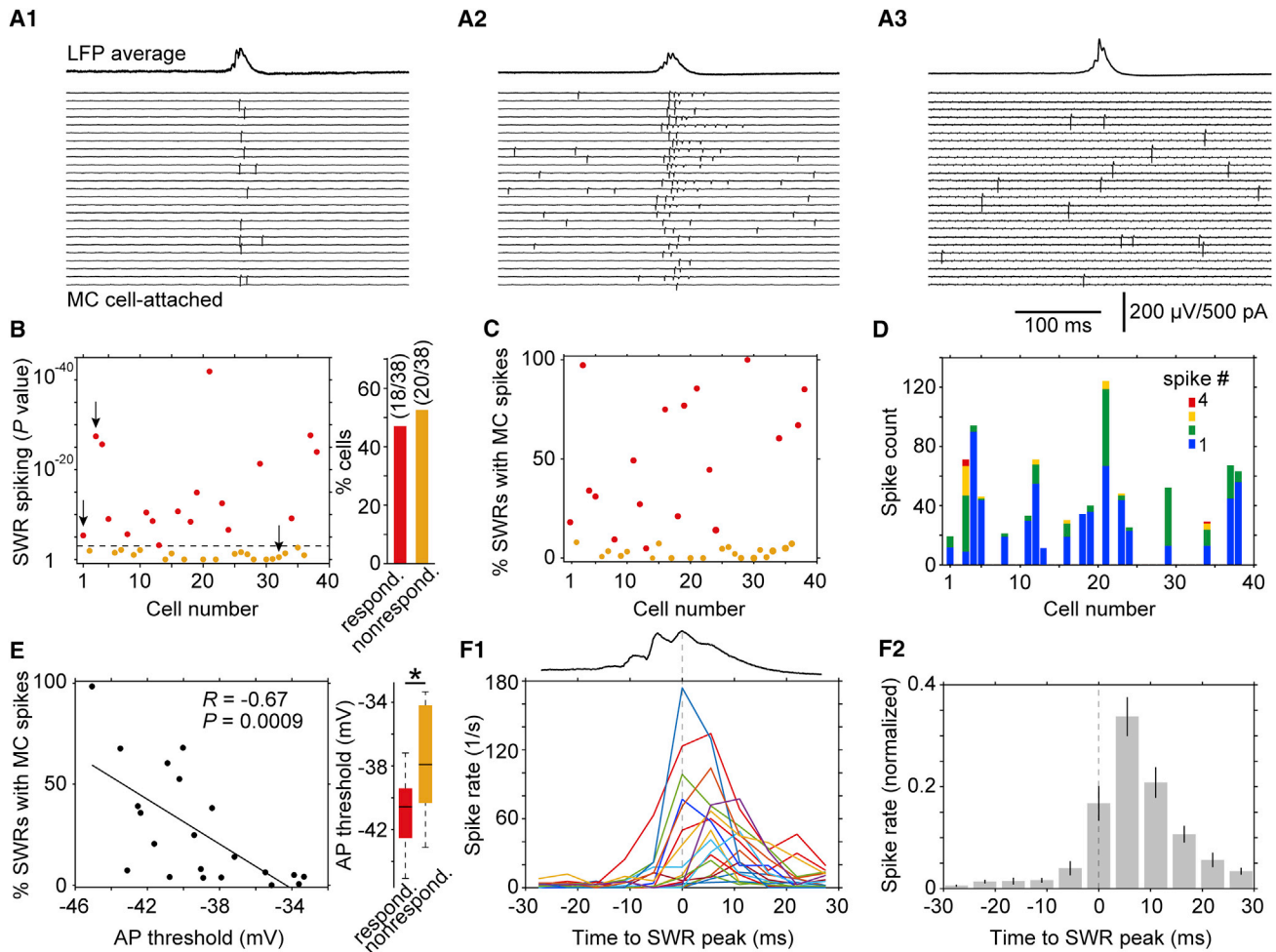
Figure 2. Analysis of MC Activity during CA3 SWRs

(A1–A3) Discharge patterns of three MCs during CA3 SWRs. Successive sweeps (25 and 400 ms) centered to the SWR peak (average top).

(B) Spiking of MCs within and outside SWR epochs was compared (Mann-Whitney U test). Left: display of p values (x axis, order of experiments). Red and orange dots indicate a significant increase (responding) or no significant increase (nonresponding) in spike rate during SWRs; dotted line, $\alpha = 0.001$; arrows, cells shown in (A1–A3). Right: distribution of responding and nonresponding MCs.

(C) Numbers of SWR epochs with MC spiking divided by total number of SWR epochs per experiment shown as percentages (x axis and color as in B).

(D) Distribution of mean spike counts per SWR for responding cells (order as in B and C).

(E) Left: correlation analysis of MC spiking and AP threshold (n = 21). Right: lower AP threshold in responding cells; error bars represent 10th and 90th percentiles.

(F1) PETHs of responding MCs, 5 ms bin size. Top: grand average SWR.

(F2) Average PETH after normalization (peak at 6.4 ms). Error bars represent SEM.

Non-invasive recordings from MCs (depth 32–80 μm; Figures S1C–S1D) revealed spontaneous and heterogeneous action potential (AP) firing as illustrated in raster plots of three cells (Figure 1B). The distribution of the overall spike rates is given in Figure 1C (mean 0.5 ± 0.1/s, median 0.2/s, range 0–3.6/s; n = 38 cells).

MCs are known to receive excitatory synaptic input at high rates, mostly from GC axons (Scharfman et al., 1990; Strowbridge et al., 1992) but potentially also from "feedback" projections originating from CA3 pyramidal neurons (Scharfman, 1994c). We asked whether the observed MC spiking could potentially reflect SWR-associated activity arising from CA3.

MC Activation during SWRs

We recorded the local field potential (LFP) in the PC layer of area CA3c (Lorente de Nó, 1934) together with activity from MCs, and we indeed observed spikes coinciding with SWRs in a substantial fraction of MCs (Figure 1D), suggesting recruitment of these neurons by population activity in the adjacent CA3.

Patterns of MC spiking observed in peri-SWR epochs are shown in Figure 2A. To statistically evaluate a causal relation between MC spiking and SWRs in CA3, we compared the spiking during SWRs with spiking during randomly sampled periods (Mann-Whitney U test; Figure 2B). Of 38 MCs, the spiking in 18 cells (47%) was significantly coupled with SWRs ("responding"),

while for the remaining cells (53%), no coupling could be found, or they were mostly silent ("nonresponding"; Figures S2A–S2E). In the responding MCs, SWR-linked spiking for individual cells varied between ~5% and 100% (Figure 2C), independent of the recording depth from the slice surface (Figure S2F). In addition, the number of spikes per SWR ranged from one to four (mean 1.4 ± 0.02; Figure 2D). We tested several intrinsic and network parameters that might account for differences in responding and nonresponding MCs. None of these measures were different (Figures S2G and S2H) with the exception of AP threshold, which was negatively correlated with SWR-related spiking (Figure 2E, left). Specifically, the AP threshold was more negative in responding MCs, implying that synaptic activity would evoke spikes at a higher probability (Figure 2E, right; p = 0.017, two-tailed unpaired t test).

We analyzed the distribution of spike times with respect to the SWR peak time as a common temporal reference across cells. Figure 2F displays the SWR-locked peri-event time histograms (PETHs), individually for all responding cells (trial-averaged spike rates; Figure 2F1) and the average after normalization (Figure 2F2). Across cells, the peak firing of MCs was delayed with respect to the SWR peak (6.4 ms; Figure 2F2), demonstrating a delayed recruitment of MCs into the active neuronal network during SWRs in the adjacent CA3 area.

SWR-Related Synaptic Inputs in MCs Are Reliable and Phase Locked

Given the substantial fraction of active MCs, we were interested in exploring the underlying synaptic activity. We sequentially recorded, from the same cells, compound excitatory postsynaptic currents (cEPSCs) and compound inhibitory postsynaptic currents (cIPSCs) (cEPSCs at −60 mV, cIPSCs at +6 mV) concurrently with CA3 SWRs. Figure 3 illustrates features of these currents: excitatory and inhibitory compound postsynaptic current (cPSC) amplitudes were in the range of several hundreds of picoamperes (cEPSCs: mean 644 ± 70 pA, median 679 pA; cIPSCs: mean 509 ± 50 pA, median 520 pA; n = 25 cells; see also Figure S3A). In addition, SWR-related cPSCs in MCs were highly reliable, with success rates of 100% and 97% for cEPSCs and cIPSCs (Figure S3A). Spectral analysis of both components revealed frequencies consistent with the ripple frequency (cEPSCs versus cIPSCs: mean 144 ± 1 Hz versus 144 ± 2 Hz, median 143 Hz versus 142 Hz, p = 0.9, Mann-Whitney U test; Figure 3B), supported by amplitude-time histograms of cPSCs indicating ~5 ms rhythmicity (Figure S3B).

We have previously shown the coherence of synaptic inputs in CA1 PCs, and in oriens-lacunosum moleculare (O-LM) interneurons with ripples *in vitro* (Maier et al., 2011; Pangalos et al., 2013; see Hájos et al., 2013, for similar results in CA3). We wondered whether such coupling was also present between CA3 ripples and related synaptic input in MCs (Figure 3C). In data obtained from 25 MCs, we found significant phase locking with the CA3 ripple for both cEPSCs and cIPSCs (p < 1 × 10^{-8} and p < 9 × 10^{-7}, Rayleigh test; Figure 3D). Comparison of the average phases revealed a lead of excitatory over inhibitory synaptic inputs (cEPSC- and cIPSC-to-ripple phase: 14.3 ± 8.2° [vector strength 0.29] versus 39.2 ± 9.9° [vector strength 0.26]; see also Figure S3C).

Scharfman (1994c) showed unitary synaptic connections from CA3 PCs onto MCs with time-to-peak latencies in the range of

3.5–8.5 ms. To quantify the propagation time of SWR-related synaptic activity to MCs, we performed cross-correlation analyses of cPSCs with CA3 SWRs. Consistent with the previously reported monosynaptic delays, we found time lags of ~5 ms for cEPSCs (mean 4.8 ± 0.3 ms, median 4.9 ms; 1,214 events; Figure 3E1), while time lags for cIPSCs were prolonged (mean 5.9 ± 0.4 ms, median 5.7 ms, 1,187 events; p = 0.0005, paired two-tailed t test; n = 25 cells; Figure 3E2).

To corroborate these propagation delays with an additional approach, we performed simultaneous recordings from PCs and MCs with the CA3 LFP. Figure 3F1 displays the ripple peak-triggered averages of SWRs and corresponding cEPSCs and cIPSCs in both a PC and an MC (green and orange; reconstructions; Figure 3F2). In 15 such recordings, we found consistently delayed cPSCs in MCs compared with PCs (cEPSC delays: mean 3.8 ± 0.5 ms, median 3.6 ms, 1,224 events; cIPSC delays: mean 5.9 ± 0.7 ms, median 5.7 ms, 1,598 events; Figure 3F3). Moreover, inhibitory latencies were prolonged compared with excitatory latencies (p = 0.006, paired two-tailed t test; Figure 3F3, bottom).

Together, these findings confirm the precise signaling and delayed propagation of ripple-related synaptic activity from the CA3 network to MCs.

SWR-Linked Excitatory Synaptic Activity Is Routed to GCs via MCs

Within the local network, MC spiking has been shown to evoke excitatory postsynaptic responses in DG GCs and in hilar interneurons (Scharfman, 1995; Larimer and Strowbridge, 2008). We were thus interested in testing whether SWR-related activity in CA3 is relayed on to GCs, potentially via active MCs. Indeed, we observed significant SWR-associated excitatory and inhibitory synaptic inputs in GCs (cEPSCs and cIPSCs: 19 of 29 [66%] and 13 of 22 [60%] GCs; Figure S4A). To investigate the timing of SWR-related synaptic activity in MCs and in GCs, we simultaneously recorded from cells of both groups, together with the CA3c LFP (Figure 4A). We found that SWR-associated cEPSCs in GCs consistently lagged behind those detected in MCs (Figures 4A2 and 4A3), with an average delay of 4.2 ± 0.6 ms (median 4.1 ms; 1,266 events in 16 simultaneous recordings; Figure 4B). This delay is consistent with prolonged cross-correlation derived LFP-cEPSC time lags determined in GCs compared with MCs (Figures S4B and S4C). It supports the idea of backpropagation of SWR-linked excitatory activity from the CA3 area to the GC/dentate network via a disynaptic pathway involving MCs.

We sought to test this hypothesis using a different approach. We reasoned that the ripple-associated population activity in CA3 might be more tightly coupled with excitatory synaptic input in MCs than in GCs, given the disynaptic chain of propagation (CA3 → MC → GC) and the reported failure rates at the MC → GC synapse (22% on average; Scharfman, 1995). We used CA3 SWR amplitude as a readout parameter of the local network excitability. In 31 slices, we correlated individual SWR amplitudes with corresponding cEPSC amplitudes in PCs (see histogram of correlation coefficients in Figure 4C1). Similarly, we obtained correlation coefficients for MCs (56 slices; Figure 4C2) and GCs (38 slices; Figure 4C3). The medians of the distributions are similar for PCs and MCs (0.58 versus 0.56; red lines) but considerably lower for GCs (0.18). We obtained
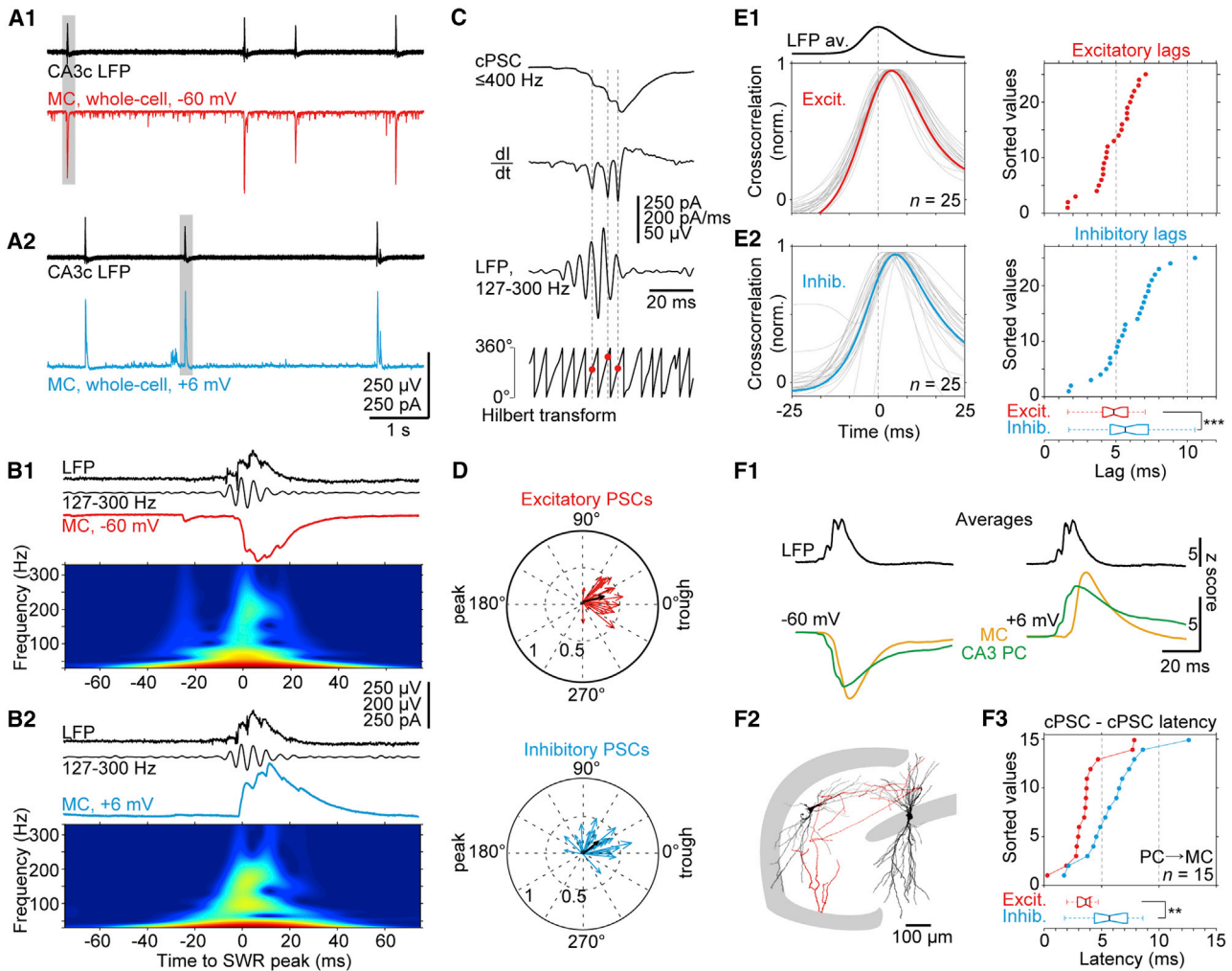
Figure 3. Timing of Ripple-Linked cPSCs in MCs

(A1 and A2) SWRs in CA3c (top) linked with cEPSCs and cIPSCs in MCs (red and blue).

(B1 and B2) Events marked in (A1) and (A2) at higher resolution; top to bottom: LFP SWR, filtered version, and cEPSC (red) and cIPSC (blue). Below: wavelet spectrograms of the cEPSC and cIPSC; warmer colors represent higher power.

(C) Analysis of cPSC-to-ripple phases. Top: time points of steepest rising slopes in cPSC identified by their first derivatives (middle). The phases of these time points were determined with respect to the ripple (LFP) using its Hilbert phase (red dots, bottom). In total, 2,770 excitatory and 3,012 inhibitory slopes were analyzed.

(D) Polar plots of average phases of excitatory (red) and inhibitory (blue) PSCs (slopes) of each cell with respect to CA3 ripples; black arrows: resultant phase vectors.

(E1 and E2) Left, cross-correlation (CC) analysis of cEPSCs (E1) and cIPSCs (E2); single (gray) and averaged (red and blue) CC functions, aligned to peak of SPW envelope (top). Right: median SPW-cPSC time lags for cEPSCs (red) and cIPSCs (blue). Bottom: cIPSCs are delayed compared with cEPSCs.

(F1–F3) Simultaneous PC-MC recordings during CA3c SWRs. (F1) Ripple peak-triggered averages of 100 SWRs (top) and their excitatory (left) and inhibitory (right) cPSCs (PC, green; MC, orange; reconstruction; F2). (F3) Median latencies for cEPSCs (red) and cIPSCs (blue). Inhibitory compared with excitatory latencies are consistently delayed in simultaneously recorded PCs and MCs (bottom).

(E2) (bottom right) and (F3) (bottom): error bars represent 10th and 90th percentiles.

transformed Fisher's *Z* values to statistically compare these data and found no difference for *Z* values representing LFP-PC and LFP-MC correlations (p = 0.94, Tukey's multiple-comparisons test), while *Z* values representing LFP-GC correlations were significantly smaller (p < 0.0001 for both comparisons, Tukey's multiple-comparisons test; Figure 4D).

Together, these results demonstrate that during SWRs, network activity is equally linked with excitatory signaling in PCs and MCs but not in GCs. This rejects a strong role for direct

functional coupling of CA3 PCs and GCs (Li et al., 1994) during ripples but supports an indirect propagation of SWR-related excitatory activity onto GCs via MCs.

DISCUSSION

Despite recent progress in elucidating their behavioral relevance (Jinde et al., 2012; Danielson et al., 2017; GoodSmith et al., 2017; Senzai and Buzsáki, 2017), MCs remain a comparatively
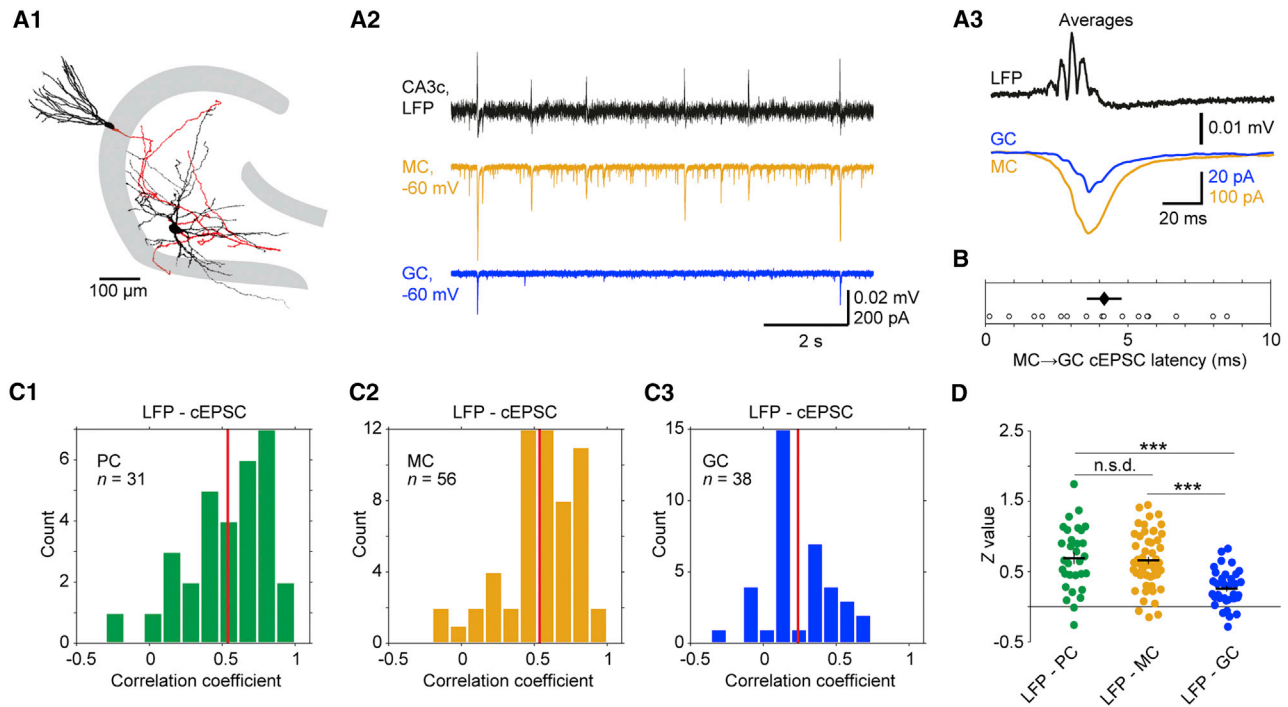
Figure 4. Ripple-Associated Functional Coupling of CA3 and GCs via MCs

(A1) Reconstruction of simultaneously recorded MC and GC.

(A2) Example sweeps, same experiment as (A1). Top: CA3 SWR and corresponding cEPSCs in MC (orange) and GC (blue).

(A3) Ripple peak-triggered average of 100 SWRs (top) and corresponding cEPSCs (as A1 and A2).

(B) Median latencies (16 MC-GC recordings; diamond, average). The error bar represents SEM.

(C1–C3) Correlation of CA3c SWR and cEPSC amplitudes in PCs (C1), MCs (C2), and GCs (C3). Histograms of Pearson correlation coefficients for amplitudes of SWRs and cEPSCs in CA3 PCs (31 slices, 2,231 SWRs; C1), MCs (56 slices, 3,695 SWRs; C2), and GCs (38 slices, 2,326 SWRs; C3). Red lines, population medians.

(D) Comparison of Fisher's Z values. Dots, Z-transformed correlation coefficients from the histograms in (C1)–(C3). Error bars represent SEM.

unexplored neuron population, especially regarding their differential role in various brain states. This is due mainly to their relatively low density deep in the hilus (1–5 MCs per 100 GCs, i.e., ~10,000 MCs in the rat; Henze and Buzsáki, 2007; Myers and Scharfman, 2009) and their particular vulnerability, which impedes *in vivo* recording and post hoc anatomical identification (Scharfman and Myers, 2013; GoodSmith et al., 2017). Here, we took advantage of an *in vitro* approach whereby SWRs can be studied in isolation and at the single-cell level to investigate MCs in a targeted way. *In vitro* SWRs share multiple properties with their *in vivo* counterparts, including their spatial and spectral profiles, pharmacology, and activation patterns of participating neurons (Maier et al., 2009; Koniaris et al., 2011; Hájos et al., 2013; Pangalos et al., 2013; for review, see Maier and Kempter, 2017).

We identified prominent excitatory postsynaptic currents in MCs that consistently followed SWRs in CA3c. This finding implies a transient functional coupling of MCs with the CA3 area during SWRs. As an anatomical substrate underlying this coupling, a monosynaptic excitatory "back-projection" from CA3 pyramidal neurons onto MCs has been demonstrated with paired intracellular recordings (Scharfman, 1994c). In these unitary connections, the time of spike to excitatory postsynaptic potential (EPSP) was comparable with the time lags we observed for CA3 LFP and cEPSCs in MCs, which we further substantiated

by simultaneous cEPSC recordings in PCs and MCs. Together, these results suggest that ensembles of rhythmically active CA3 pyramidal neurons directly provide input to MCs during SWRs.

Beside phase-locked excitatory cPSCs, we observed pronounced, phase-locked inhibitory cPSCs in MCs. Their time lags with respect to the LFP were prolonged compared with those of excitatory cPSCs. The inhibitory delays were confirmed by latencies determined in simultaneous cIPSC recordings from PCs and MCs.

Several possible explanations are conceivable for the origin of ripple-locked inhibition in MCs. (1) Recently, a novel class of GABAergic interneurons was shown to send axons from CA1/CA3 to the DG and to increase spiking during SWRs (Szabo et al., 2017). (2) In addition to these "boundary-crossing" projections, it is feasible that MCs are targeted by CA3 interneurons that are known to discharge during ripples, namely, basket, bistratified, and O-LM cells (Lasztóczi et al., 2011; Hájos et al., 2013; Tukker et al., 2013). (3) The recruitment of local hilar interneurons (Sík et al., 1997; Hosp et al., 2014) by axon collaterals of CA3 PCs constitutes another possibility. In this framework, spiking CA3 PCs activate hilar interneurons that in turn provide inhibition in MCs, as the output of a disynaptic pathway (PC → interneuron → MC). However, given the large amplitudes and

the ripple phase coupling of cIPSCs in MCs, (1) and (2) seem to be the more likely explanations.

Synaptic inputs in MCs evoked by population activity generated in CA3 have been studied *in vitro* before, but in the context of experimentally enhanced cellular excitability or epileptiform activity (Scharfman, 1994a, 1994b; Hedrick et al., 2017). Epileptiform discharges, compared with SWR activity, exhibit considerably enhanced amplitude, duration, multi-unit activity, and oscillation frequency (Karlócai et al., 2014; Aivar et al., 2014). Thus, profound differences exist between the network mechanisms that govern pathological network discharges as opposed to physiological SWRs.

We found significant activation in 47% of probed MCs, which is in contrast to the previously reported low activation of CA3 PCs during SWRs (Hájos et al., 2013). What could explain the discrepancy in the activation of these two neighboring principal neuron populations during SWRs? A characteristic feature of MCs is an ongoing "bombardment" with excitatory synaptic activity, at rates considerably higher than in CA3 PCs (Scharfman and Schwartzkroin, 1988; Strowbridge et al., 1992). This background activity might serve as an excitatory "blanket," raising the likelihood of spiking during SWRs. In addition, Scharfman and Schwartzkroin (1988) demonstrated higher input resistance in MCs than in CA3 PCs, which contributes to cellular excitability and hence a more likely recruitment of MCs during SWRs.

Although not addressed directly so far, recent work has provided indirect evidence for MC activation during SWRs: MCs are active during SWS (Senzai and Buzsáki, 2017), which is the sleep stage characterized by a high occurrence of SWRs in the hippocampus. Our observations *in vitro* support this finding and demonstrate that the SWR-associated increased network excitability is sufficient to drive MCs.

What could be consequences of MC spiking in the neuronal network? Previous research has shown that dentate GCs, a major neural population targeted by MCs (Scharfman, 1995, 1996), are also active during SWRs (Buzsáki, 1986; Ylinen et al., 1995) and SWS (Senzai and Buzsáki, 2017). In awake mice, Hulse and colleagues (2017) have directly shown that GCs depolarize during SWRs.

We hypothesize that the discharge of MCs relays SWR-related activity to GCs, thereby contributing to the activation of these neurons. First, this reasoning is in agreement with our observation that excitatory synaptic inputs in GCs are often coupled with SWRs. Second, it is in line with the consistent delay between ripple-related cPSCs in GCs and simultaneously recorded MCs. And third, this is supported by strong correlations between CA3 SWR amplitudes and cEPSC amplitudes in both PCs and MCs, but not in GCs, demonstrating a direct connection of the CA3 excitatory oscillation generator driving PCs and MCs, but importantly not GCs. All these findings support a disynaptic chain of activity propagation (CA3 PC → MC → GC; Scharfman, 1994b).

MCs are part of an excitatory recurrent feedback network (Lisman, 1999) and placed in a strategic position to integrate information from the connected neuronal sub-networks, DG and CA3. MCs receive converging excitatory inputs from CA3 PCs and GCs and send projections in an eminently divergent fashion: ipsilaterally, along the septotemporal axis of the hippocampus,

MC axons can span hundreds of micrometers, with a greater concentration of proximal contacts in the hilus, presumably on interneurons (Larimer and Strowbridge, 2008), as opposed to an aggregation of more distant contacts in the inner molecular layer, presumably on GCs (Buckmaster et al., 1996). As a consequence, proximal GCs might be predominantly suppressed by MC-driven disynaptic inhibition (Buzsáki and Eidelberg 1981; Buckmaster et al., 1996), in contrast to distal GCs, which may be entrained by enhanced MC activity during SWRs. SWR-linked MC spiking might represent the physiological trigger to induce long-term potentiation (LTP) at the MC → GC synapse, as shown for experimental activation of MC axons (Hashimotodani et al., 2017). Contralaterally, MC axons contribute to commissural terminals linking both hippocampi (Berger et al., 1981; Ribak et al., 1985; Hsu et al., 2016). It is tempting to speculate that the active MCs support, or mediate, the SWR-related synchronization of hippocampus along the septotemporal axis (Patel et al., 2013) or across hemispheres at the timescale of several milliseconds (Buzsáki, 1986; Buzsáki et al., 2003). Given the prominent innervation of GABAergic interneurons by MCs, this synchronization could be mediated by local and/or contralateral inhibitory neurons (Scharfman, 1995; Larimer and Strowbridge, 2008; Hsu et al., 2016).

Together, these features suggest the role of MCs as a neuronal hub linking local and distal compartments of both hippocampi in a complex manner. Our findings on the "feedback" recruitment of MCs strongly argue for a central role of these cells in SWR-related hippocampal functions, which include the consolidation of spatial and emotional memories (Jinde et al., 2012; Myers and Scharfman, 2009; Scharfman, 2016).

EXPERIMENTAL PROCEDURES

Animal maintenance and experiments followed institutional guidelines, the guidelines of the Berlin state (T0100/03), and European Union (EU) Council Directive 2010/63/EU on the protection of animals used for experimental and other scientific purposes. Male C57BL/6N mice (3–5 weeks of age) were used.

Slice Preparation and Electrophysiology

Horizontal slices of ventral to mid-hippocampus were prepared as described before (Maier et al., 2009). Slices were stored in an interface chamber, and combined LFP and patch-clamp (cell-attached or whole-cell) recordings were performed at 31°C–32°C in a submerged-type recording chamber.

Data Analysis

SWR detection was performed in MATLAB (The MathWorks) as described before (Maier et al., 2009). Time windows of 300 ms (55 ms for spike analysis) aligned to the peak of identified SWRs were cut out from LFP and corresponding intracellular traces and were baseline-corrected by subtracting the respective means. Digital filtering was performed with second-order Butterworth filter at the indicated frequencies.

Spike times were detected using a threshold algorithm (8 × SD of the spike-free baseline). To quantify SWR-related spiking, the number of spikes in n SWR epochs of 55 ms centered on the ripple maxima were determined. This dataset (N_1) was compared with spiking in n periods of identical duration (N_2) randomly sampled from the entire spike train, including periods with SWR epochs (Mann-Whitney U test; $\alpha = 0.001$). As a result, MCs were classified as responding or nonresponding during SWRs. The SWR maximum is the temporal reference in PETHs (bin width 5 ms; Figure 2F). The sum of spike counts S per time bin was divided by the sum m of SWRs observed and the bin width Δt,

indicating spike rates (SR = S/m/Δt, i.e., the probability to observe a spike in a single trial for the chosen 5 ms time interval).

Individual synaptic inputs during cPSCs were detected by a derivative-peak time method (Figures 3C, S3B, and S3C): SWR-related cEPSCs and inverted cIPSCs were low-pass-filtered at 400 Hz and the derivative calculated. Of all derivative minima detected within a 60 ms window centered on the maximum of the ripple, the strongest 10% (i.e., 10% steepest slopes) were accepted as synaptic inputs. LFP signals were filtered at 127–300 Hz. Envelope and phase of the filtered signals were obtained by applying the Hilbert transform. The phase of excitatory or inhibitory inputs was determined as the respective Hilbert phase of the LFP at the time point of the steepest slopes. For each cell, an average phase vector described by its phase angle and strength was determined; the polar plots represent the resultant phase vectors of all analyzed cells.

Timing of cPSCs in double recordings was analyzed in a window of 15 ms surrounding the SWR maximum. Only significant SWR-related inputs were considered, and their delays at the time points of half-maximum amplitudes determined (see also Figures S3A and S4A).

The time-dependent power spectrum of the signal was computed using Morlet wavelet transform (Torrence and Compo, http://atoc.colorado.edu/research/wavelets/). Data are plotted as log(1 + power). Frequency at maximum power is defined as the local maximum in the 127–300 Hz range.

Statistical analysis was performed in MATLAB or GraphPad Prism (GraphPad Software). Data are reported as mean ± SEM or as medians. Box plots display the median and margin of error as the 10th and 90th percentiles. Comparisons were made using the two-tailed unpaired or paired t test, the Mann-Whitney U test, or ANOVA. The uniformity of phase angles was tested using Rayleigh's test with the CircStat toolbox (Berens, 2009). Fisher's Z transform was applied before comparing populations of correlation coefficients (Bortz and Schuster, 2010). Statistical significance is given as exact p values, with $\alpha \leq 0.05$ regarded as significant, unless stated otherwise.

SUPPLEMENTAL INFORMATION

Supplemental Information includes Supplemental Experimental Procedures and four figures and can be found with this article online at https://doi.org/10.1016/j.celrep.2018.04.095.

AUTHOR CONTRIBUTIONS

Conceptualization, D.S. and N.M.; Formal Analysis, A.S., N.M, and I.W.; Investigation, A.S. and N.M.; Resources, D.S.; Data Curation, I.W., A.S, and N.M.; Writing – Original Draft, N.M.; Writing – Review & Editing, A.S., I.W., D.S., and N.M.; Visualization, N.M. and A.S.; Project Administration, N.M., D.S., and A.S.; Funding Acquisition, D.S. and N.M.

DECLARATION OF INTERESTS

The authors declare no competing interests.

REFERENCES

Acsády, L., Katona, I., Martínez-Guijarro, F.J., Buzsáki, G., and Freund, T.F. (2000). Unusual target selectivity of perisomatic inhibitory cells in the hilar region of the rat hippocampus. J. Neurosci. 20, 6907–6919.

Aivar, P., Valero, M., Bellistri, E., and Menendez de la Prida, L. (2014). Extracellular calcium controls the expression of two different forms of ripple-like hippocampal oscillations. J. Neurosci. 34, 2989–3004.

Amaral, D.G. (1978). A Golgi study of cell types in the hilar region of the hippocampus in the rat. J. Comp. Neurol. 182, 851–914.

Berens, P. (2009). CircStat: a MATLAB toolbox for circular statistics. J. Stat. Softw. 31, 1–21.

Berger, T.W., Semple-Rowland, S., and Basset, J.L. (1981). Hippocampal polymorph neurons are the cells of origin for ipsilateral association and commissural afferents to the dentate gyrus. Brain Res. 215, 329–336.

Bortz, J., and Schuster, C. (2010). Statistik für Human- und Sozialwissenschaftler, Seventh Edition (Berlin-Heidelberg, Germany: Springer-Verlag).

Both, M., Bähner, F., von Bohlen und Halbach, O., and Draguhn, A. (2008). Propagation of specific network patterns through the mouse hippocampus. Hippocampus 18, 899–908.

Buckmaster, P.S., Strowbridge, B.W., and Schwartzkroin, P.A. (1993). A comparison of rat hippocampal mossy cells and CA3c pyramidal cells. J. Neurophysiol. 70, 1281–1299.

Buckmaster, P.S., Wenzel, H.J., Kunkel, D.D., and Schwartzkroin, P.A. (1996). Axon arbors and synaptic connections of hippocampal mossy cells in the rat in vivo. J. Comp. Neurol. 366, 271–292.

Buzsáki, G. (1986). Hippocampal sharp waves: their origin and significance. Brain Res. 398, 242–252.

Buzsáki, G. (2015). Hippocampal sharp wave-ripple: a cognitive biomarker for episodic memory and planning. Hippocampus 25, 1073–1188.

Buzsáki, G., and Eidelberg, E. (1981). Commissural projection to the dentate gyrus of the rat: evidence for feed-forward inhibition. Brain Res. 230, 346–350.

Buzsáki, G., Buhl, D.L., Harris, K.D., Csicsvari, J., Czéh, B., and Morozov, A. (2003). Hippocampal network patterns of activity in the mouse. Neuroscience 116, 201–211.

Danielson, N.B., Turi, G.F., Ladow, M., Chavlis, S., Petrantonakis, P.C., Poirazi, P., and Losonczy, A. (2017). In vivo imaging of dentate gyrus mossy cells in behaving mice. Neuron 93, 552–559.e4.

Frotscher, M., Seress, L., Schwerdtfeger, W.K., and Buhl, E. (1991). The mossy cells of the fascia dentata: a comparative study of their fine structure and synaptic connections in rodents and primates. J. Comp. Neurol. 312, 145–163.

Girardeau, G., Benchenane, K., Wiener, S.I., Buzsáki, G., and Zugaro, M.B. (2009). Selective suppression of hippocampal ripples impairs spatial memory. Nat. Neurosci. 12, 1222–1223.

GoodSmith, D., Chen, X., Wang, C., Kim, S.H., Song, H., Burgalossi, A., Christian, K.M., and Knierim, J.J. (2017). Spatial representations of granule cells and mossy cells of the dentate gyrus. Neuron 93, 1–14.

Hájos, N., Ellender, T.J., Zemankovics, R., Mann, E.O., Exley, R., Cragg, S.J., Freund, T.F., and Paulsen, O. (2009). Maintaining network activity in submerged hippocampal slices: importance of oxygen supply. Eur. J. Neurosci. 29, 319–327.

Hájos, N., Karlócai, M.R., Németh, B., Ulbert, I., Monyer, H., Szabó, G., Erdélyi, F., Freund, T.F., and Gulyás, A.I. (2013). Input-output features of anatomically identified CA3 neurons during hippocampal sharp wave/ripple oscillation in vitro. J. Neurosci. 33, 11677–11691.

Hashimotodani, Y., Nasrallah, K., Jensen, K.R., Chávez, A.E., Carrera, D., and Castillo, P.E. (2017). LTP at hilar mossy cell-dentate granule cell synapses modulates dentate gyrus output by increasing excitation/inhibition balance. Neuron 95, 928–943.e3.

Hedrick, T.P., Nobis, W.P., Foote, K.M., Ishii, T., Chetkovich, D.M., and Swanson, G.T. (2017). Excitatory synaptic input to hilar mossy cells under basal and hyperexcitable conditions. eNeuro 4 (6), ENEURO.0364-17.2017.

34

Henze, D.A., and Buzsáki, G. (2007). Hilar mossy cells: functional identification and activity in vivo. Prog. Brain Res. *163*, 199–216.

Henze, D.A., Urban, N.N., and Barrionuevo, G. (2000). The multifarious hippocampal mossy fiber pathway: a review. Neuroscience *98*, 407–427.

Hosp, J.A., Strüber, M., Yanagawa, Y., Obata, K., Vida, I., Jonas, P., and Bartos, M. (2014). Morpho-physiological criteria divide dentate gyrus interneurons into classes. Hippocampus *24*, 189–203.

Hsu, T.T., Lee, C.T., Tai, M.H., and Lien, C.C. (2016). Differential recruitment of dentate gyrus interneuron types by commissural versus perforant pathways. Cereb. Cortex *26*, 2715–2727.

Hulse, B.K., Lubenov, E.V., and Siapas, A.G. (2017). Brain state dependence of hippocampal subthreshold activity in awake mice. Cell Rep. *18*, 136–147.

Jadhav, S.P., Kemere, C., German, P.W., and Frank, L.M. (2012). Awake hippocampal sharp-wave ripples support spatial memory. Science *336*, 1454–1458.

Jinde, S., Zsiros, V., Jiang, Z., Nakao, K., Pickel, J., Kohno, K., Belforte, J.E., and Nakazawa, K. (2012). Hilar mossy cell degeneration causes transient dentate granule cell hyperexcitability and impaired pattern separation. Neuron *76*, 1189–1200.

Karlócai, M.R., Kohus, Z., Káli, S., Ulbert, I., Szabó, G., Máté, Z., Freund, T.F., and Gulyás, A.I. (2014). Physiological sharp wave-ripples and interictal events in vitro: what's the difference? Brain *137*, 463–485.

Koniaris, E., Drimala, P., Sotiriou, E., and Papatheodoropoulos, C. (2011). Different effects of zolpidem and diazepam on hippocampal sharp wave-ripple activity in vitro. Neuroscience *175*, 224–234.

Kowalski, J., Geuting, M., Paul, S., Dieni, S., Laurens, J., Zhao, S., Drakew, A., Haas, C.A., Frotscher, M., and Vida, I. (2010). Proper layering is important for precisely timed activation of hippocampal mossy cells. Cereb. Cortex *20*, 2043–2054.

Kubota, D., Colgin, L.L., Casale, M., Brucher, F.A., and Lynch, G. (2003). Endogenous waves in hippocampal slices. J Neurophysiol. *89*, 81–89.

Larimer, P., and Strowbridge, B.W. (2008). Nonrandom local circuits in the dentate gyrus. J. Neurosci. *28*, 12212–12223.

Lasztóczi, B., Tukker, J.J., Somogyi, P., and Klausberger, T. (2011). Terminal field and firing selectivity of cholecystokinin- expressing interneurons in the hippocampal CA3 area. J Neurosci. *31*, 18073–18093.

Lee, A.K., and Wilson, M.A. (2002). Memory of sequential experience in the hippocampus during slow wave sleep. Neuron *36*, 1183–1194.

Li, X.G., Somogyi, P., Ylinen, A., and Buzsáki, G. (1994). The hippocampal CA3 network: an in vivo intracellular labeling study. J. Comp. Neurol. *339*, 181–208.

Lisman, J.E. (1999). Relating hippocampal circuitry to function: recall of memory sequences by reciprocal dentate-CA3 interactions. Neuron *22*, 233–242.

Lorente de Nó, R. (1934). Studies on the structure of the cerebral cortex. II. Continuation of the study of the ammonic system. J. Psychol. Neurol. *46*, 113–177.

Maier, N., Nimmrich, V., and Draguhn, A. (2003). Cellular and network mechanisms underlying spontaneous sharp wave-ripple complexes in mouse hippocampal slices. J. Physiol. *550*, 873–887.

Maier, N., Morris, G., Johenning, F.W., and Schmitz, D. (2009). An approach for reliably investigating hippocampal sharp wave-ripples in vitro. PLoS ONE *4*, e6925.

Maier, N., Tejero-Cantero, A., Dorrn, A.L., Winterer, J., Beed, P.S., Morris, G., Kempter, R., Poulet, J.F.A., Leibold, C., and Schmitz, D. (2011). Coherent phasic excitation during hippocampal ripples. Neuron *72*, 137–152.

Maier, N., and Kempter, R. (2017). Hippocampal Sharp Wave/Ripple Complexes—Physiology and Mechanisms. In Cognitive Neuroscience of Memory Development, N. Axmacher and B. Rasch, eds. (Switzerland: Springer International Publishing), pp. 227–249.

Myers, C.E., and Scharfman, H.E. (2009). A role for hilar cells in pattern separation in the dentate gyrus: a computational approach. Hippocampus *19*, 321–337.

Neunuebel, J.P., and Knierim, J.J. (2012). Spatial firing correlates of physiologically distinct cell types of the rat dentate gyrus. J. Neurosci. *32*, 3848–3858.

Pangalos, M., Donoso, J.R., Winterer, J., Zivkovic, A.R., Kempter, R., Maier, N., and Schmitz, D. (2013). Recruitment of oriens-lacunosum-moleculare interneurons during hippocampal ripples. Proc. Natl. Acad. Sci. U S A *110*, 4398–4403.

Papatheodoropoulos, C., and Kostopoulos, G. (2002). Spontaneous GABA(A)-dependent synchronous periodic activity in adult rat ventral hippocampal slices. Neurosci. Lett. *319*, 17–20.

Patel, J., Schomburg, E.W., Berényi, A., Fujisawa, S., and Buzsáki, G. (2013). Local generation and propagation of ripples along the septotemporal axis of the hippocampus. J. Neurosci. *33*, 17029–17041.

Ribak, C.E., Seress, L., and Amaral, D.G. (1985). The development, ultrastructure and synaptic connections of the mossy cells of the dentate gyrus. J. Neurocytol. *14*, 835–857.

Scharfman, H.E. (1994a). Synchronization of area CA3 hippocampal pyramidal cells and non-granule cells of the dentate gyrus in bicuculline-treated rat hippocampal slices. Neuroscience *59*, 245–257.

Scharfman, H.E. (1994b). EPSPs of dentate gyrus granule cells during epileptiform bursts of dentate hilar "mossy" cells and area CA3 pyramidal cells in disinhibited rat hippocampal slices. J. Neurosci. *14*, 6041–6057.

Scharfman, H.E. (1994c). Evidence from simultaneous intracellular recordings in rat hippocampal slices that area CA3 pyramidal cells innervate dentate hilar mossy cells. J. Neurophysiol. *72*, 2167–2180.

Scharfman, H.E. (1995). Electrophysiological evidence that dentate hilar mossy cells are excitatory and innervate both granule cells and interneurons. *74*, 179–194.

Scharfman, H.E. (1996). Conditions required for polysynaptic excitation of dentate granule cells by area CA3 pyramidal cells in rat hippocampal slices. Neuroscience *72*, 655–668.

Scharfman, H.E. (2016). The enigmatic mossy cell of the dentate gyrus. Nat. Rev. Neurosci. *17*, 562–575.

Scharfman, H.E., and Myers, C.E. (2013). Hilar mossy cells of the dentate gyrus: a historical perspective. Front. Neural Circuits *6*, 106.

Scharfman, H.E., and Schwartzkroin, P.A. (1988). Electrophysiology of morphologically identified mossy cells of the dentate hilus recorded in guinea pig hippocampal slices. J. Neurosci. *8*, 3812–3821.

Scharfman, H.E., Kunkel, D.D., and Schwartzkroin, P.A. (1990). Synaptic connections of dentate granule cells and hilar neurons: results of paired intracellular recordings and intracellular horseradish peroxidase injections. Neuroscience *37*, 693–707.

Senzai, Y., and Buzsáki, G. (2017). Physiological properties and behavioral correlates of hippocampal granule cells and mossy cells. Neuron *93*, 691–704.e5.

Sík, A., Penttonen, M., and Buzsáki, G. (1997). Interneurons in the hippocampal dentate gyrus: an in vivo intracellular study. Eur. J. Neurosci. *9*, 573–588.

Soriano, E., and Frotscher, M. (1994). Mossy cells of the rat fascia dentata are glutamate-immunoreactive. Hippocampus *4*, 65–69.

Strowbridge, B.W., Buckmaster, P.S., and Schwartzkroin, P.A. (1992). Potentiation of spontaneous synaptic activity in rat mossy cells. Neurosci. Lett. *142*, 205–210.

Szabo, G.G., Du, X., Oijala, M., Varga, C., Parent, J.M., and Soltesz, I. (2017). Extended interneuronal network of the dentate gyrus. Cell Rep. *20*, 1262–1268.

Tukker, J.J., Lasztóczi, B., Katona, L., Roberts, J.D.B., Pissadaki, E.K., Dalezios, Y., Márton, L., Zhang, L., Klausberger, T., and Somogyi, P. (2013). Distinct dendritic arborization and in vivo firing patterns of parvalbumin-expressing basket cells in the hippocampal area CA3. J. Neurosci. *33*, 6809–6825.

Ylinen, A., Soltész, I., Bragin, A., Penttonen, M., Sík, A., and Buzsáki, G. (1995). Intracellular correlates of hippocampal theta rhythm in identified pyramidal cells, granule cells, and basket cells. Hippocampus *5*, 78–90.

Supplemental Information

Involvement of Mossy Cells

in Sharp Wave-Ripple Activity *In Vitro*

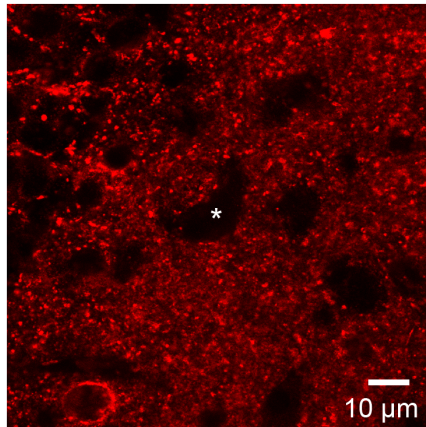Aarti Swaminathan, Ines Wichert, Dietmar Schmitz, and Nikolaus Maier

Inventory of Supplemental Information
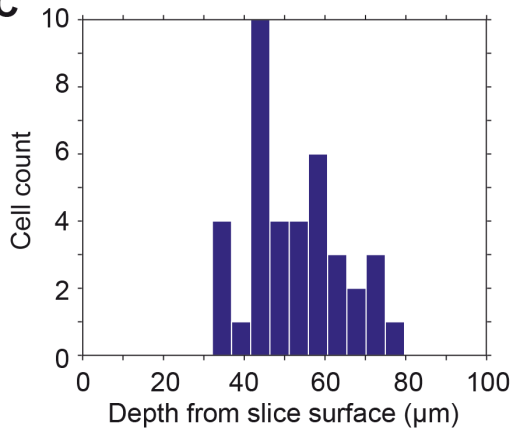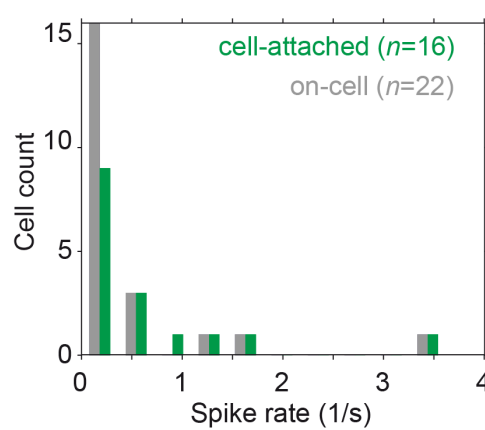
The Supplemental Information contains the following items:

Supplemental Figures S1 – S4; these figures add information related to the respective figures shown in the main part of the manuscript

**Supplemental Experimental Procedures** – a section detailing experimental methods

A

B

Intrinsic physiological properties of mossy cells

Resting membrane potential (mV)*	-60.1 ± 1.4
Input resistance (MΩ)	312.8 ± 30.7
Action potential	
Threshold (mV)	-40.0 ± 0.8
Amplitude (mV)	70.5 ± 2.8
Duration at 50% of AP maximum (ms)	0.9 ± 0.03
Afterhyperpolarization amplitude (mV)	6.5 ± 0.8
Sag potential amplitude (mV)	7.0 ± 0.8

*no LJP correction; Values are expressed as mean ± S.E.M.; n = 12 MCs N = 7 mice
95% CIs: RMP: [-63.1 mV -57.1 mV]; Ri: [245.3 MΩ 380.4 MΩ]; AHP: [4.7 mV 8.3 mV]

C

D

Figure S1. Additional analyses of mossy cell properties. Related to Figure 1.

A GAD67 staining demonstrates the absence of this inhibitory marker on MCs in our sample. The *asterisk* marks the cell displayed in the main Figure 1A. **B** Intrinsic physiological properties of the recorded MCs (n = 12). *Initial resting membrane potential* (RMP) was determined in current-clamp immediately after rupturing the cell membrane. *Input resistance* (R_i) was calculated based on -4 mV steps (50 ms duration) in voltage-clamp, repeated 100 times to minimize the influence of spontaneous synaptic inputs. Trace segments of 10 ms duration with minimal SDs for baseline and steady-state were chosen, averaged, and their means subtracted (ΔI). The voltage step size (-4 mV) was then divided by ΔI to calculate the cell's R_i. *Action potential* (AP) parameters were determined from spikes recorded at rheobase. *AP threshold*, V_{thres}: the membrane potential where dV/dt of the rising phase exceeded 20 mV/ms; *peak amplitude* of APs: measured from V_{thres} to the peak; *width* of APs: the time difference between the points where the rising- and the decaying phases of the AP crossed 50% of its peak amplitude; *afterhyperpolarization* amplitude: the voltage difference between V_{thres} and the most negative deflection immediately following the peak of the AP; *sag potential* amplitude: the voltage difference between the minimum voltage in response to the current injection (-120 pA, 1 s) from the RMP and the steady-state response. **C** Histogram showing the depth distribution of the recorded cells from the surface of the slice (range: 32 to 80 µm). **D** Comparison of the *overall* spike rates, *i.e.*, the total number of spikes divided by the recording time of the individual experiment (on-cell recordings: mean: 0.44 ± 0.12/s; median: 0.08/s, n = 22 cells, N = 11 mice; cell-attached recordings: mean: 0.66 ± 0.22/s; median: 0.3/s, n = 16 cells, N = 9 mice; not different, P = 0.067, two-tailed Mann-Whitney U test).
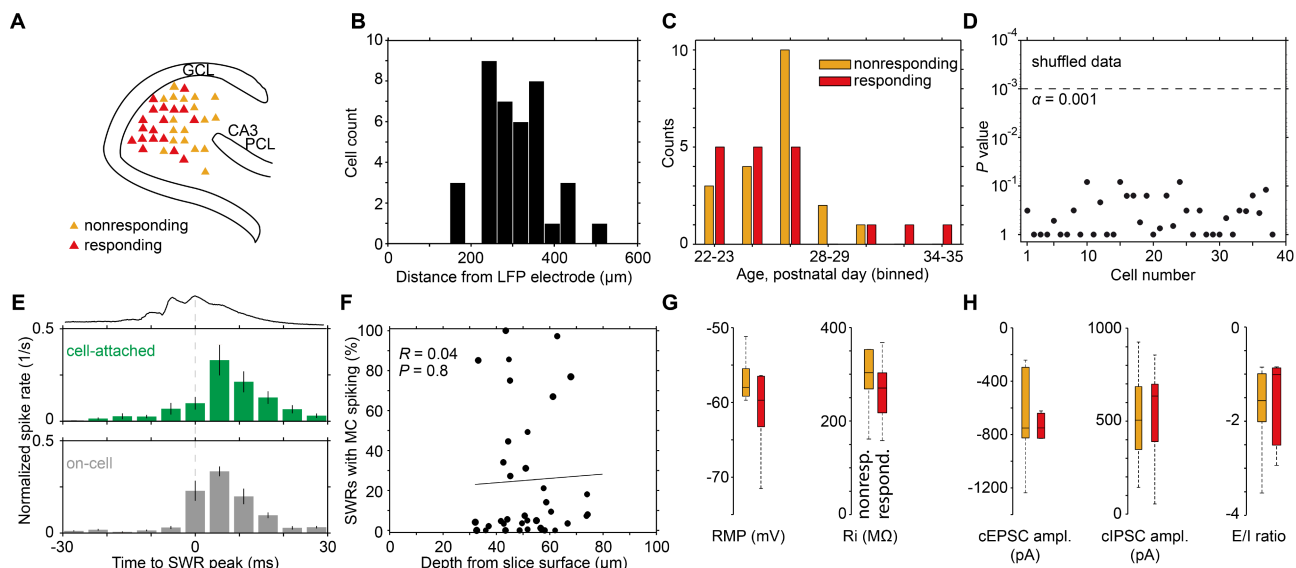
Figure S2. Analysis of SWR-related spiking in MCs in vitro. Related to Figure 2.
A Sketch of the recording location within the hilus of analyzed MCs. *Abbreviations:* GCL, granule cell layer; PCL, pyramidal cell layer.
B Histogram summarizing the distribution of distances between the LFP electrode in CA3c and the recorded MCs (range: 149 to 529 μm). For all cell-attached recordings, data of at least 6 min after GΩ seal formation were discarded to ensure stabilization of the LFP. **C** Histogram of responding and nonresponding MCs within the range of ages tested (P 22-35; each bin represents the sum of observations in two days). **D** Control related to the analysis shown in the main Figure 2B. Comparison of spiking in shuffled data: In each cell, two spike distributions *N1* and *N2* of *n* randomly sampled periods from the entire trace (where *n* matched the number of detected SWRs in the respective experiment) were compared (Mann-Whitney *U* test). The distribution of *P* values lies clearly above the chosen significance threshold $\alpha = 0.001$, demonstrating the robustness of SWR-related spiking in MCs (see main Figure 2B) against data shuffling. Values are plotted according to the order of recordings (*x*-axis, as in the main Figure 2B-C). **E** Plots related to the histogram shown in the main Figure 2F to demonstrate the spike-time distribution with reference to the SWR peak (LFP average, *top*); however, here, data were separated according to the recording technique applied (*green:* cell-attached, and *grey:* on-cell). **F** No correlation between SWR-related spiking and depth of the recordings was found. **G and H** Comparisons of different intrinsic and synaptic parameters in responding (resp.) and nonresponding (nonresp.) cells; an unpaired nonparametric test (Mann Whitney *U* test) was applied in all cases. **G** *Left*: Resting membrane potential (RMP, $P = 0.25$, $n = 10$ and $n = 11$ for responding and nonresponding cells). *Right:* Input resistance (R$_i$, $P = 0.32$, $n = 10$ and $n = 10$ for responding and nonresponding cells). **H** *Left*: SWR-associated cEPSC amplitudes ($P = 0.67$, $n = 7$ and $n = 11$ for responding and nonresponding cells); *Middle:* SWR-associated cIPSC amplitudes ($P = 0.81$, $n = 7$ and $n = 11$ for responding and nonresponding cells); *Right*: For each cell, charge transfer values of excitatory and inhibitory SWR-associated PSCs were determined and their ratios plotted (E/I ratio, $P = 0.54$, $n = 7$ and $n = 11$ for responding and nonresponding cells).
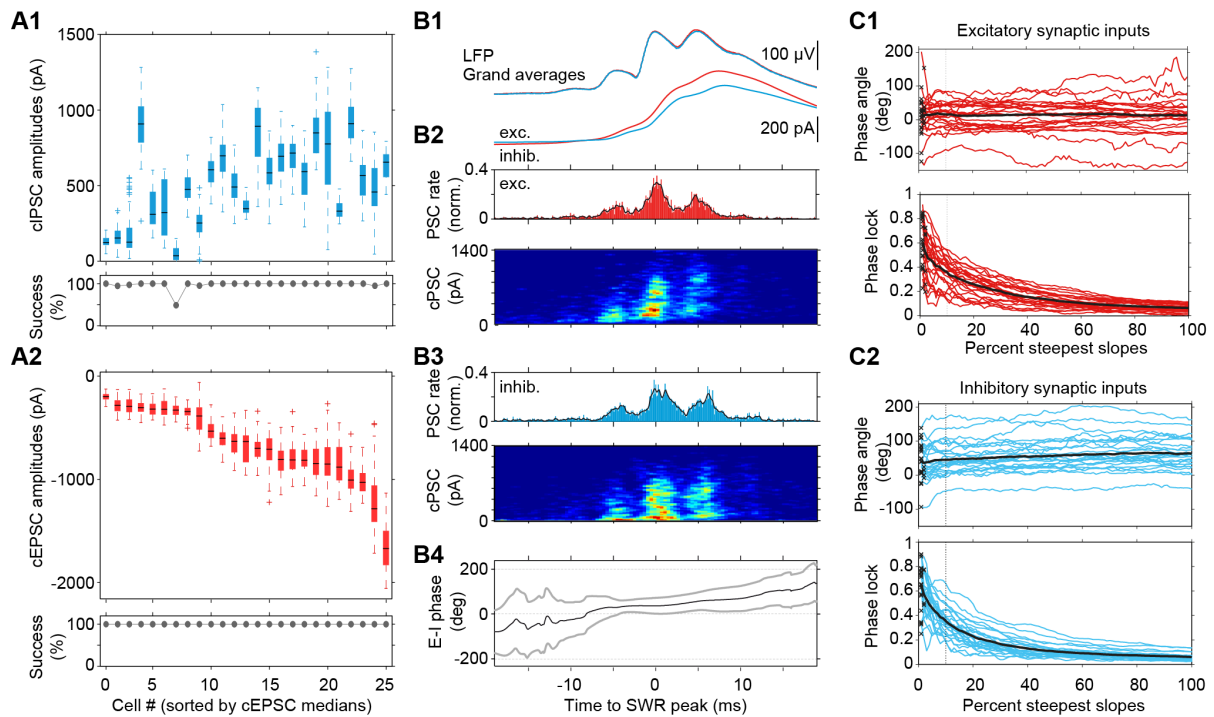
Figure S3. Amplitude and phase analysis of ripple-associated cPSC in MCs. Related to Figure 3.

A Peak current amplitudes of SWR-associated cIPSCs (recorded at +6 mV, **A1**, *top*) and cEPSCs (recorded at -60 mV, **A2**, *top*) were sorted by the medians of cEPSC amplitudes; *Bottom:* observation likelihoods (success rates) of cIPSCs and cEPSCs. We statistically compared the current trace surrounding the SWR peak (-20 ms to +45 ms) with a concatenated current trace containing data clearly separate from the given SWR event (-120 ms to -20 ms, and +45 ms to +120 ms with respect to the SWR peak; 175 ms duration in total). An unpaired two-sample, one-tailed *t* test, with α set to 0.1 was applied (right- and left-tailed testing for cEPSCs and cIPSCs, respectively). If the null hypothesis was rejected at $\alpha = 0.1$, the current sweep was classified as containing a synaptic event caused by the given SWR event, otherwise it was categorized uncoupled. For both, excitatory and inhibitory cPSCs, high success rate values were found. **B1** Grand averages, *upper* traces show LFPs, and *lower* the respective cPSCs, for excitatory (*red*, inverted) and inhibitory (*blue*) events. The ripple peak is the time reference in *B1-B4* (time point zero in *B4*). **B2 and B3** *Upper*: histograms (binsize = 0.1 ms, 400 bins) of the time points of the 10% strongest slopes of synaptic inputs, for excitatory (*B2*) and inhibitory (*B3*) PSCs. For all cells, the mean histogram over events was generated and normalized, corresponding to the empirical time-dependent input rate (number of inputs/ms). The resulting histograms were averaged and additionally smoothed with a Gaussian kernel (*black lines,* variance 0.2 ms). *Lower*: Amplitude-time histograms: Following the detection of the steepest slopes, the absolute amplitudes within the cPSCs were defined as the maximum values of the raw signal in the interval between the steepest increase (*i.e.*, the peak of the cPSC derivative) and the onset of the next synaptic input (*i.e.*, the following minimum of the cPSC derivative). The data were then binned in 2D histograms: The *x*-axis is the time difference of the steepest increase and the maximum peak of the LFP ripple signal as in the upper histogram (binsize 0.4 ms, 100 bins). The *y*-axis is the absolute amplitude (binsize 14 pA, 100 bins). The histogram was smoothed by convolution with a 2D Gaussian kernel (kernel width=1.5 bins; variance: 0.6 ms in *x*-axis and 21 pA in *y*-axis). To average over all cells, a histogram was generated for each cell with the sum over all bins normalized to 1, and then the average of all individual histograms was calculated. **B4** Temporal evolution of cEPSC-to-cIPSC phase difference. The excitatory and inhibitory traces were averaged and their Hilbert phases subtracted for each slice (*Grey lines*, SD). The cEPSC-to-cIPSC phase difference increased by 27.4° within the course of the LFP ripple (*i.e.* from -5 to +5 ms with respect to the ripple peak), corresponding to 0.53 ms on average (assuming 143 Hz median oscillation frequency in MC cEPSCs, as estimated by wavelet analysis; see main text). **C** Dependence of resulting phase and phase lock on the proportion of included events: a relative threshold was defined to decide whether a slope should be accepted as synaptic input or not, so that it would cover a fixed proportion of the possible extrema. To determine a reasonable value for this proportion, for all cells (**C1**, excitatory events; **C2**, inhibitory events), the average phase (*upper panel*) and phase lock (*lower panel*) were calculated for varying proportions (*x*-axis). Crosses denote the percentage for each cell that corresponds to 50 considered events; the *bold black lines* represent the averages over cells. *Dotted lines* correspond to the used proportion of events (10%). The average phase is robust with respect to changes in this percentage. The proportion of 10% was therefore chosen for the following two reasons: First, it is large enough to include a sufficient number of events (>50) for each cell; second, the phase lock at this percentage is high, indicating a low number of false-positive extrema.
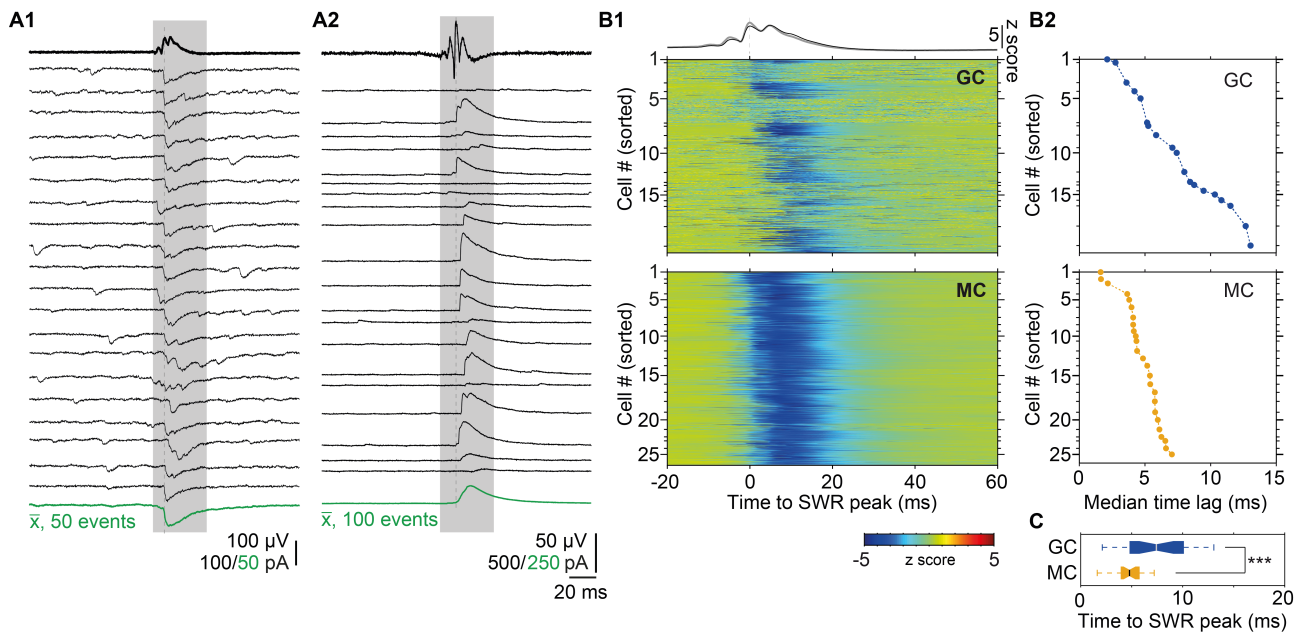
Figure S4. SWR-associated synaptic inputs in dentate gyrus GCs. Related to Figure 4.

A Examples displaying excitatory and inhibitory synaptic activity in GCs during CA3 SWRs in two independent recordings. Twenty successive sweeps of cEPSCs (V_{hold}, -60 mV, **A1**) and cIPSCs (V_{hold}, +6 mV, **A2**), centered on the peak of CA3 SWRs. *Green traces:* average of 50 and 100 sweeps for cEPSCs and cIPSCs, respectively. Synaptic inputs in GCs associated with SWRs are smaller on average than those observed in MCs. To separate spontaneous (not SWR-associated) and SWR-associated synaptic inputs, we used the following unbiased procedure to identify 'significant', *i.e.*, SWR-driven synaptic responses. We considered periods of 2 s centered on the maximum of the ripple peak (127-300 Hz filtered signal). Following baseline offset correction, the current sweeps were divided into 20 ms bins and the mean values were determined in each of the resulting 100 bins. With these values, a matrix of dimension 100× the number of SWR events in the given recording was created, where the row dimension corresponded to time and the column dimension corresponded to sweep numbers. Using repeated measures one-way ANOVA, all columns were pairwise compared. If the values in the SWR-related column were determined larger than those in the surrounding columns (determined with Tukey's *post-hoc* test at a level of $\alpha = 0.05$), the given cell was categorized as significantly modulated by SWR-related activity. Even in significantly modulated GCs, we found a high variability in amplitudes of both excitatory and inhibitory synaptic inputs (see examples in the main Figure 4). **B1** Color plots of individual SWR-modulated baseline-corrected cEPSC events in GCs (*above, n* = 19) and MCs (*below, n* = 25) displayed from -20 ms to 60 ms with respect to the SWR peak (*top:* z-scored grand averages of CA3 SWRs (black and grey) recorded simultaneously with GCs and MCs, respectively). The color bar (*bottom*) represents the z-scored amplitude values of cEPSCs. Cells were sorted according to their median time lag as shown in panel *B2*. The numbers of recorded cEPSCs varied between cells and hence the spacing between *y*-axis ticks is not equidistant. **B2** As for the analysis displayed in the main Figure 3E1, excitatory and inhibitory PSCs were low-pass filtered at 100 Hz (2nd order Butterworth filter) and cross-correlated with the corresponding envelope of 100 Hz low-pass filtered SWRs (xcorr function in Matlab). The distribution of sorted cross-correlation derived median LFP-cEPSC time lags in GCs (*top*) and MCs (*bottom,* same as in the main Fig. 3E1) is displayed, corresponding to the colorplots shown in *B1*. **C** Comparison of median LFP-cEPSC time lags. SWR-cEPSC time lags are significantly prolonged in GCs compared to MCs (*P* = 0.0008, unpaired two-tailed *t* test).

41

Supplemental Experimental Procedures

Slice preparation. Following isoflurane-anesthesia, brains were transferred to ice-cold sucrose-based ACSF containing (in mM): 87 NaCl, 2.5 KCl, 3 $MgCl_2 \cdot 6H_2O$, 0.5 $CaCl_2$, 10 glucose, 50 sucrose, 1.25 NaH_2PO_4, and 26 $NaHCO_3$ (pH 7.4). Horizontal slices (400 μm) of ventral to mid-hippocampus were cut on a vibratome (VT1200S, Leica) and stored in an interface chamber perfused with ACSF containing (in mM): 119 NaCl, 2.5 KCl, 1.3 $MgCl_2$, 2.5 $CaCl_2$, 10 glucose, 1.25 NaH_2PO_4, and 26 $NaHCO_3$, at pH 7.4; osmolarity of 290 to 310 mosmol/l. The temperature was kept at ~32°C, and slices were superfused at a rate of ~1 ml/min. ACSF was equilibrated with carbogen (95% O_2, 5% CO_2). Slices recovered for >1.5 h after preparation.

Electrophysiology. Recordings were done in ACSF at 31-32°C in a submerged-type recording chamber perfused at 5-6 ml/min (Maier et al., 2009). For LFP recordings, glass microelectrodes (tip opening ~5-10 μm; 0.2-0.3 MΩ) were filled with ACSF. Whole-cell recordings were done with glass electrodes (2-5 MΩ) filled with either of two solutions containing (in mM): *(i)* 120 K-gluconate, 10 HEPES, 10 KCl, 5 EGTA, 2 $MgSO_4 \cdot 7H_2O$, 3 MgATP, 1 Na_2GTP, 14 phosphocreatine, and 5.4 biocytin (0.2 %); pH adjusted to 7.4 with KOH, or *(ii)* 117.5 gluconic acid, 8 NaCl, 10 TEA, 10 HEPES, 0.2 EGTA, 5 QX-314, 2.5 CsCl, 0.3 Na_2GTP, and 4 MgATP, 5.4 biocytin (0.2%); pH adjusted to 7.4 with CsOH. MC spiking was recorded for at least 10 min either in the cell-attached configuration (voltage clamp, VC, at -60 mV) using solution *(i)* or in on-cell recordings using ACSF-filled patch pipettes.

LFPs were amplified 1000× and whole-cell data were amplified 5× for VC and 10× for current-clamp recordings using a Multiclamp 700A or B amplifier (Molecular Devices). Data were low-pass filtered at 4 kHz (Bessel filter) and digitized at 20 kHz with 16-bit resolution using an A/D converter (BNC-2090 board, National Instruments, or Axon Digidata 1550A, Molecular Devices). Data were stored using Igor Pro (Wavemetrics) or pClamp (Molecular Devices). Series resistance (R_s) was monitored continuously; recordings were rejected if R_s exceeded 20 MΩ or varied >30%. No R_s compensation was used; no liquid junction potential correction was applied. For on-cell recordings, a candidate MC was chosen, and an ACSF-filled patch pipette placed on its soma. After recording of a sufficient amount of data, the pipette was removed and the cell re-approached with another pipette filled with intracellular solution and subsequently recorded in the whole-cell configuration, as described above.

Immunostainings and anatomical identification. Cells were routinely filled with 0.2% biocytin and slices were transferred to 4% paraformaldehyde for at least 3 h and maintained at 4° C in 0.1 M phosphate-buffered

saline (PBS) with 0.1% sodium-azide. For immunostainings, slices were washed 3× with 0.1 M PBS. The slices were blocked with 5% normal goat serum, followed by overnight incubation with streptavidin (1:500, Invitrogen) and mouse anti-GAD67 Ab (1:500, Millipore) at 4° C. Slices were then washed 3× in 0.1M PBS and incubated in Alexa 488 goat anti-mouse secondary Ab (1:500, Invitrogen), and Alexa 647 goat anti-mouse Ab (1:500, Invitrogen) for 2-4 h at room temperature. After washes in 0.1 M PBS, slices were mounted on slides and embedded in a mounting medium (Mowiol). Maximum intensity z-stack images were taken using a confocal microscope (Leica DMI 6000) with a 20× oil immersion objective. Reconstructions were done using the Simple Neurite tracer plugin in ImageJ (V 1.51).

Terminology. Hippocampal sharp waves (SPWs; Buzsáki, 1986) and ripples (O'Keefe and Nadel, 1978) were first characterized in behaving rats as fundamental signatures of normal EEG. However, the term *sharp wave* is also used in the context of clinical literature signifying a specific EEG graphoelement related to interictal epileptiform discharges (IED; Niedermeyer, 2005). Even though mechanistic properties, oscillation frequency, and information content carried by PC discharge during SWRs change in epilepsy (Aivar et al., 2014; Karlócai et al., 2014; Valero et al., 2017), physiological and epileptic sharp waves/ripples are likely to form a continuum of electrographic patterns expressed by the hippocampal network. Based on these studies, we follow a terminology where *sharp waves* (*SPWs*) and *ripples* (or *sharp wave-ripple complexes*, *SWRs*) refer to physiological activity patterns as opposed to IED and *fast ripples* or pathological ripples (*p-ripples*) (see also Traub and Whittington, 2010; Buzsáki, 2015).

References

Aivar, P., Valero, M., Bellistri, E., Menendez de la Prida, L. (2014). Extracellular calcium controls the expression of two different forms of ripple-like hippocampal oscillations. J Neurosci *34*, 2989–3004.

Buzsáki, G. (1986). Hippocampal sharp waves: Their origin and significance. Brain Res *398*, 242–252.

Buzsáki, G. (2015). Hippocampal sharp wave-ripple: A cognitive biomarker for episodic memory and planning. Hippocampus *25*, 1073–1188.

Karlócai, M.R., Kohus, Z., Káli, S., Ulbert, I., Szabó, G., Máté, Z., Freund, T.F., Gulyás, A.I. (2014). Physiological sharp wave-ripples and interictal events in vitro: What's the difference? Brain *137*, 463–485.

Maier, N., Morris, G., Johenning, F.W., Schmitz, D. (2009). An approach for reliably investigating hippocampal sharp wave-ripples in vitro. PLoS ONE *4*, e6925.

Niedermeyer, E. (2005). Abnormal EEG Patterns: Epileptic and Paroxysmal. In Electroencephalography Basic Principles, Clinical Applications, and Related Fields. Niedermeyer, E. and Lopes da Silva, F.H. ed. (Philadelphia, USA: Lippincott Williams & Wilkins), pp. 255–280.

O'Keefe, J. and Nadel, L. (1978). The hippocampus as a cognitive map. (Oxford: Oxford University Press).

Traub, R.D. and Whittington, M.A. (2010). Cortical Oscillations in Health and Disease (Oxford: Oxford University Press).

Valero, M., Averkin, R.G., Fernandez-Lamo, I., Aguilar, J., Lopez-Pigozzi, D., Brotons-Mas, J.R., Cid, E., Tamás, G., Menendez de la Prida, L. (2017). Mechanisms for selective single-cell reactivation during offline sharp-wave ripples and their distortion by fast ripples. Neuron *94*, 1234–1247.

Journal Data Filtered By: Selected JCR Year: 2017 Selected Editions: SCIE,SSCI Selected Categories: 'CELL BIOLOGY' Selected Category Scheme: WoS

Rank	Full Journal Title	Total Cites	Journal Impact Factor	Eigenfactor Score
1	NATURE REVIEWS MOLECULAR CELL BIOLOGY	43,667	35.612	0.095540
2	NATURE MEDICINE	75,461	32.621	0.171980
3	CELL	230,625	31.398	0.583260
4	Cell Stem Cell	23,493	23.290	0.096030
5	CANCER CELL	35,217	22.844	0.096910
6	Cell Metabolism	29,834	20.565	0.101740
7	NATURE CELL BIOLOGY	39,896	19.064	0.092960
8	TRENDS IN CELL BIOLOGY	13,708	18.564	0.037630
9	Science Translational Medicine	26,691	16.710	0.126450
10	CELL RESEARCH	13,728	15.393	0.037450
11	MOLECULAR CELL	61,604	14.248	0.181170
12	NATURE STRUCTURAL & MOLECULAR BIOLOGY	27,547	13.333	0.081820
13	Autophagy	14,923	11.100	0.035510
14	MEDICINE	9,213	11.021	0.019720
15	EMBO JOURNAL	67,036	10.557	0.079780
16	CURRENT OPINION IN CELL BIOLOGY	13,339	10.015	0.027790
17	DEVELOPMENTAL CELL	26,896	9.616	0.074980
18	GENES & DEVELOPMENT	57,469	9.462	0.092720
19	CURRENT BIOLOGY	56,595	9.251	0.137200
20	Cold Spring Harbor Perspectives in Biology	13,275	9.247	0.049360
21	Annual Review of Cell and Developmental Biology	9,812	9.032	0.016870
22	Cell Systems	1,129	8.982	0.009600
23	AGEING RESEARCH REVIEWS	5,297	8.973	0.012030
24	JOURNAL OF CELL BIOLOGY	68,915	8.784	0.085170
25	EMBO REPORTS	13,293	8.749	0.031350
26	PLANT CELL	48,393	8.228	0.063640
27	MATRIX BIOLOGY	4,803	8.136	0.008500
28	Cell Reports	29,789	8.032	0.210690
29	CELL DEATH AND DIFFERENTIATION	18,865	8.000	0.031540
30	AGING CELL	8,067	7.627	0.018910
31	CURRENT OPINION IN STRUCTURAL BIOLOGY	10,619	7.179	0.024320
32	ONCOGENE	66,411	6.854	0.075960
33	CELLULAR AND MOLECULAR LIFE SCIENCES	23,341	6.721	0.041340
34	Stem Cell Reports	4,525	6.537	0.026290
35	CYTOKINE & GROWTH FACTOR REVIEWS	5,668	6.395	0.008050

12. Curriculum vitae

My curriculum vitae does not appear in the electronic version of my paper
for reasons of data protection.

My curriculum vitae does not appear in the electronic version of my paper
for reasons of data protection.

13. Complete list of publications

1. **Swaminathan A**, Wichert I, Schmitz D, Maier N. (2018) Involvement of Mossy Cells in Sharp Wave-Ripple Activity In Vitro. *Cell Rep. 23(9):2541-2549.*

2. Burk K, Ramachandran B, Ahmed S, Hurtado-Zavala JI, Awasthi A, Benito E, Faram R, Ahmad H, **Swaminathan A**, McIlhinney J, Fischer A, Perestenko P, Dean C. (2017) Regulation of Dendritic Spine Morphology in Hippocampal Neurons by Copine-6. *Cereb Cortex. 2017 Feb 3:1-18.*

14. Acknowledgments